



Retrieving H₂O/HDO columns over cloudy and clear-sky scenes from the Tropospheric Monitoring Instrument (TROPOMI)

Andreas Schneider^{1,a}, Tobias Borsdorff¹, Joost aan de Brugh¹, Alba Lorente¹, Franziska Aemisegger², David Noone³, Dean Henze⁴, Rigel Kivi⁵, and Jochen Landgraf¹

¹Earth science group, SRON Netherlands Institute for Space Research, Utrecht, the Netherlands

²Atmospheric Dynamics group, Department of Environmental Systems Science, ETH Zürich, Zürich, Switzerland

³Department of Physics, University of Auckland, Auckland, New Zealand

⁴Department of Ocean, Earth and Atmospheric Sciences, Oregon State University, Corvallis, Oregon, United States of America

⁵Earth Observation Research Unit, Finnish Meteorological Institute, Sodankylä, Finland

^aNow at: Earth Observation Research Unit, Finnish Meteorological Institute, Sodankylä, Finland

Correspondence: Andreas Schneider (andreas.schneider@fmi.fi), Tobias Borsdorff (t.borsdorff@sron.nl)

Abstract. This paper presents an extension of the scientific HDO/H₂O column data product from the Tropospheric Monitoring Instrument (TROPOMI) including clear-sky and cloudy scenes. The retrieval employs a forward model which accounts for scattering, and the algorithm infers the trace gas column information, surface properties and effective cloud parameters from the observations. The extension to cloudy scenes greatly enhances coverage, particularly enabling data over oceans. The data set is validated against co-located ground-based Fourier transform infrared (FTIR) observations by the Total Carbon Column Observing Network (TCCON). The median bias for clear-sky scenes is 1.4×10^{21} molec cm⁻² (2.9 %) in H₂O columns and 1.1×10^{17} molec cm⁻² (-0.3 %) in HDO columns, which corresponds to -17‰ (9.9 %) in a posteriori δD . The bias for cloudy scenes is 4.9×10^{21} molec cm⁻² (11 %) in H₂O, 1.1×10^{17} molec cm⁻² (7.9 %) in HDO, and -20‰ (9.7 %) in a posteriori δD . At low-altitude stations in low and middle latitudes the bias is small, and has a larger value at high latitude stations. At high altitude stations, an altitude correction is required to compensate for different partial columns seen by the station and the satellite. The bias in a posteriori δD after altitude correction depends on sensitivity due to shielding by clouds, and on realistic prior profile shapes for both isotopologues. Cloudy scenes generally involve low sensitivity below the clouds, and since the information is filled up by the prior, it plays an important role in these cases. Over oceans, aircraft measurements with the Water Isotope System for Precipitation and Entrainment Research (WISPER) instrument from a field campaign in 2018 are used for validation, yielding a bias of -3.9 % in H₂O and -3‰ in δD over clouds. To demonstrate the added value of the new data set, a short case study of a cold air outbreak over the Atlantic Ocean in January 2020 is presented, showing the daily evolution of the event with single overpass results.

1 Introduction

Atmospheric moisture strongly controls Earth's radiative budget and transports energy via latent heat, e.g. from low to high latitudes. Uncertainties in the quantification of these two effects are still large and represent one of the key uncertainties in



current climate prediction (Stevens and Bony, 2013). Isotopologues of water offer further insights into the water cycle due to fractionation processes on phase changes. This provides additional constraints for models and thus valuable insights for their improvement. The application of isotopic effects to this end requires observations on global scale and with a long-term perspective, where satellite observations from space are most promising (Rast et al., 2014).

25 HDO and H₂O are observed from space mainly in the thermal infrared spectral range, e. g. by the Infrared Atmospheric Sounding Interferometer (IASI) onboard the MetOP satellites (Herbin et al., 2009; Schneider and Hase, 2011; Schneider et al., 2016; Lacour et al., 2012) or the Atmospheric Infrared Sounder (AIRS) onboard the NASA Aqua satellite (Worden et al., 2019) which builds on earlier work using the Tropospheric Emission Spectrometer (TES) on the NASA Aura satellite (Worden et al., 2012). These sounders can observe clear-sky and cloudy scenes over land and oceans, but they are insensitive to the boundary
30 layer. The short-wave infrared (SWIR) spectral range does provide sensitivity to the boundary layer and is suitable to estimate total columns, however bodies of water are very dark in the SWIR which makes retrievals over oceans impossible for clear-sky conditions. The Tropospheric Monitoring Instrument (TROPOMI) onboard the Sentinel 5 Precursor (S5P) satellite launched on 13 October 2017 (Veefkind et al., 2012) will, together with its successor instrument Sentinel 5 on MetOp-SG-A, provide measurements in the SWIR beyond the year 2040 with unprecedented spatial resolution of 7 km × 7 km (upgraded to 5.5 km ×
35 7 km in August 2019) in the centre of the swath, daily global coverage and superior radiometric performance. Schneider et al. (2020) have recently published a first clear-sky data set of H₂O and HDO columns from TROPOMI. However, the restriction to clear-sky scenes over land hinders hydrological studies: cloudy-sky conditions are often different from clear-sky conditions, and oceans are important for the hydrological cycle. In order to extend the coverage to cloudy scenes, and therewith also to oceans, an updated retrieval is employed which accounts for scattering and estimates effective cloud parameters additionally
40 to the trace gases. Any loss of sensitivity to the partial column below the cloud is notified by the retrieval algorithm to improve data interpretation.

Isotopological abundance variations are often described by the so-called δ notation which denotes the relative difference of the ratio of the heavy and the light isotopologue, $R_{\text{HDO}} = c_{\text{HDO}}/c_{\text{H}_2\text{O}}$, to the standard abundance ratio of Vienna Standard Mean Ocean Water (VSMOW) $R_{\text{HDO, std}} = 3.1152 \times 10^{-4}$, i. e.

$$45 \quad \delta D = \frac{R_{\text{HDO}} - R_{\text{HDO, std}}}{R_{\text{HDO, std}}} \quad (1)$$

(Craig, 1961b; Hagemann et al., 1970). This nomenclature is also used herein.

Section 2 describes the retrieval setup, detailing the changes compared to the previous clear-sky-only data product by Schneider et al. (2020). Section 3 introduces reference data used for validation and intercomparison, namely ground-based Fourier transform infrared (FTIR) observations over land and aircraft measurements over the ocean. Section 4 shows validation results, with low-altitude and high-altitude FTIR stations presented separately. A comparison to the clear-sky data product by Schneider et al. (2020) for the same ground pixels is also included. Over the ocean, the retrievals are compared to aircraft measurements. Section 5 presents applications of the new data set on the global scale as well as locally for single overpasses. Finally, Sec. 6 gives a summary and conclusions.



2 Retrieval method

55 This work employs the Shortwave Infrared CO Retrieval (SICOR) algorithm, which utilises a profile-scaling approach; it is described in detail by Scheepmaker et al. (2016), Landgraf et al. (2016) and Borsdorff et al. (2014). While the clear-sky retrieval by Schneider et al. (2020) employs a forward model which ignores scattering (hereafter non-scattering retrieval), the update presented herein uses a forward model which does account for scattering using the Practical Improved Flux Method (PIFM, Zdunkowski et al., 1980) and is termed scattering retrieval hereafter. The target trace gases H₂O and HDO are fitted together
60 with the interfering species CH₄ and CO and a Lambertian surface albedo in the spectral window from 2354.0 nm to 2380.5 nm (Scheepmaker et al., 2016). The isotopologue H₂¹⁸O is included in the forward model but not fitted. Scattering cross-sections are taken from the high-resolution transmission molecular absorption database (HITRAN) 2016 release (Gordon et al., 2017). A priori profiles of water vapour are taken from the European Centre for Medium-Range Weather Forecasts (ECMWF) analysis product. Since the ECMWF data product does not distinguish individual isotopologues, H₂O, HDO and H₂¹⁸O profiles are
65 obtained from the water vapour profile by scaling it with the respective average relative natural abundances. That implicitly corresponds to a prior of δD of 0‰. A case study for high-altitude stations in Sec. 4.2 alternatively uses HDO prior profiles computed from H₂O profiles via an assumed more realistic δD profile which linearly decreases from −100‰ at the surface to −600‰ at 15 km altitude followed by a linear increase to −400‰ at the top of the atmosphere as used by Scheepmaker et al. (2016) for their simulated measurements. From this δD profile, a δ¹⁸O profile is computed via the global meteoric water line

$$70 \quad \delta D = 8 \delta^{18}O + 10‰ \quad (2)$$

(Craig, 1961a) and used to obtain the H₂¹⁸O prior profile from the H₂O profile. A priori profiles of CH₄ and CO are taken from TM5 simulations (Krol et al., 2005).

Clouds are modelled by a single scattering layer with a triangular height profile in extinction coefficient centred at cloud centre height h with a geometrical half-width d and a cloud optical thickness of τ , deploying a two-stream model. The idea is
75 to infer these effective cloud parameters from deviations of the retrieved methane column to the prior, as such differences are supposed to originate from light path modifications by scatterers. Fitting both d and τ would lead to ambiguities, thus the cloud geometric thickness d is fixed at 2500 m. The sensitivity of the inferred cloud parameters on the actual choice of d is relatively small. The approach of the CO product (Landgraf et al., 2016), which comprises fitting h and τ simultaneous to the trace gases in its spectral range 2315–2338 nm, cannot directly be transferred to the spectral window 2354–2380.5 nm because it introduces
80 errors in the inferred water vapour columns, maybe due to interferences and/or inaccuracies of the methane spectroscopy in the latter window. Thus, the effective cloud parameters are determined in a pre-fit in the spectral window from 2310 nm to 2338 nm where large absorption features of methane not interfering with water vapour are present. The resulting parameters are taken over to the final fit in the spectral window from 2354.0 nm to 2380.5 nm, where they are fixed while the trace gases are fitted. This neglects the spectral dependence of the cloud optical thickness in the spectral range between 2310 nm and 2380 nm.
85 Figure 1 visualises the spectral windows employed for the retrieval in plots of simulated transmission spectra of the relevant absorbers.

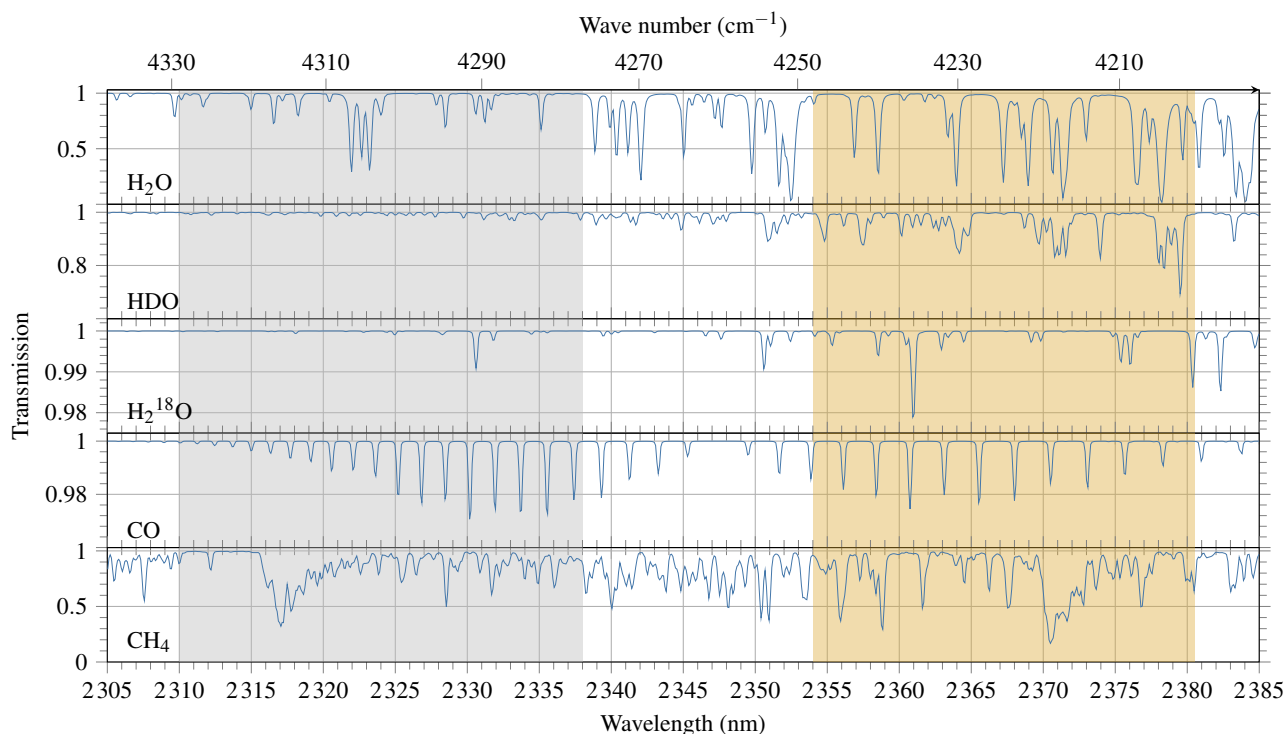


Figure 1. Simulation of atmospheric transmission in the spectral range of TROPOMI's SWIR channel for the absorbers taken into account by the retrieval algorithm. The grey shading marks the spectral window used for the determination of effective cloud parameters, the yellow shading the spectral window for the retrieval of the trace gases.

A priori surface albedos are taken from a one-year average over the year 2018 of the non-scattering product on an equal-area grid with 5760×2880 bins (corresponding to a resolution of 0.125° at the equator). Values over oceans and lakes (where the non-scattering retrieval does not yield data) are set to 0 as water is very dark in the short-wave infrared. Figure 2 shows a map of this prior. To reduce interferences with cloud parameters and stabilise the inversion, the surface albedo is slightly regularised to the prior. Regularisation in the context of ill-posed problems is discussed in detail by Borsdorff et al. (2014).

The results are filtered for convergence and with a quality filter based on fit quality in terms of the number of iterations and χ^2 as measure for the residual. Moreover, scenes with high solar zenith angles larger than 70° are filtered out since they are prone to errors. These errors are on one hand due to multi-scattering and diffraction effects not covered well by the two-stream forward model, and on the other hand due to typically low radiances resulting in low signal-to-noise ratios. From the remaining data, scenes are classified as clear-sky, cloudy with low clouds, or other (e. g. high clouds) based on retrieved effective cloud parameters as specified in Tab. 1. Only scenes of the first two categories (i. e. clear-sky or low clouds) are considered in this study and recommended to be taken into account by the user, except if the data are assimilated using averaging kernels. Clear-sky scenes are additionally filtered for surface albedo because low surface albedos usually involve low signal-to-noise ratios.

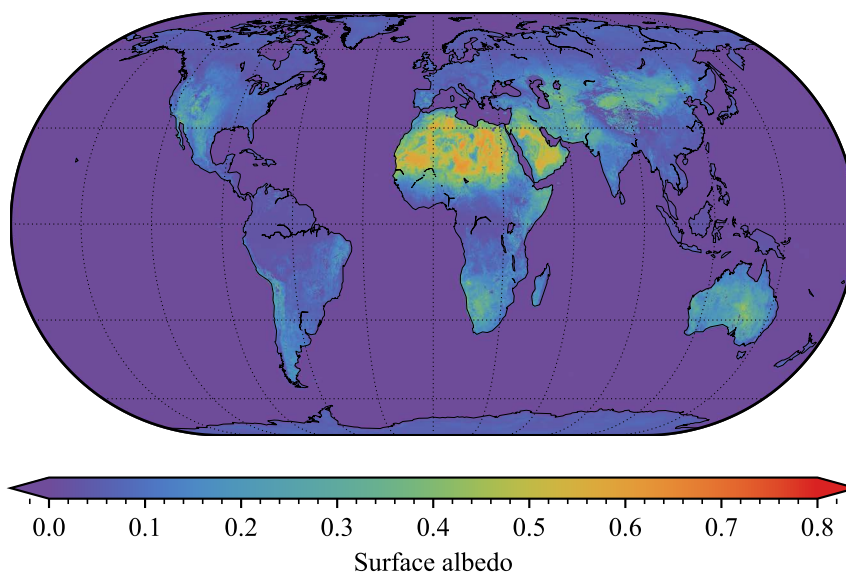


Figure 2. Average surface albedo from the non-scattering retrieval (Schneider et al., 2020) of the year 2018, which is used as a priori surface albedo for the scattering retrieval. Values over oceans and lakes (where the non-scattering retrieval does not yield data) are set to 0.

Table 1. Quality filters and selection criteria for clear-sky and cloudy-sky conditions.

Quantity	Filter
Quality filter (all scenes)	
Number of iterations	$n \leq 10$
Reduced χ^2	$\chi_f^2 \leq 150$
Reduced χ^2 of pre-fit	$\chi_p^2 \leq 150$
Solar zenith angle	$\vartheta \leq 70^\circ$
Clear-sky filter	
Cloud optical thickness	$\tau_{\text{cld}} < 0.3$
Surface albedo	$a \geq 0.02$
Filter for cloudy scenes	
Cloud height	$h_{\text{cld}} \leq 2000\text{m}$
Cloud optical thickness	$\tau_{\text{cld}} > 0.3$



100 Such a surface albedo filter is not applied to cloudy scenes because clouds usually have high reflectivity and shield the surface, which allows to retrieve over very low surface albedos with high signal-to-noise ratio.

Retrievals over optically thick clouds are insensitive to the partial column below the cloud. The algorithm estimates the missing information from the prior, however that can deviate from the truth. This requires a thorough data interpretation using the column averaging kernel, which indicates the vertical retrieval sensitivity. It can be used, e. g., to assimilate the data with
105 models to help with the interpretation when sensitivity is low.

3 Reference data

3.1 Ground-based measurements by TCCON and co-location criteria

To validate the new satellite data set, ground-based Fourier transform infrared (FTIR) observations by the Total Carbon Column Observing Network (TCCON, Wunch et al., 2011), version GGG2014 are used. The TCCON HDO data are bias-corrected by
110 dividing the HDO columns by a correction factor of 1.0778 as derived by Schneider et al. (2020). This correction accounts for a missing calibration. Table 2 lists the stations that are used for the validation.

An FTIR instrument has sensitivity in its viewing direction (i. e. in direction of the sun). If the sun is low in the sky (i. e. for high solar zenith angles), this translates into an azimuthal dependency of sensitivity, while there is no azimuthal dependency if the sun is in the zenith. To take this into account, the spatial co-location considers satellite overpasses in a cone in FTIR
115 viewing direction with an opening angle α and a radius r_α depending on solar zenith angle ϑ . Varying the opening angle linearly with SZA from α_0 at $\vartheta = 90^\circ$ to 360° at $\vartheta = 0^\circ$ and requiring equal co-location area in all cases gives

$$\alpha(\vartheta) = \alpha_{90} + \frac{90^\circ - \vartheta}{90^\circ} (360^\circ - \alpha_{90}) \quad (3)$$

$$r_\alpha = \sqrt{\frac{360^\circ}{\alpha}} r_0. \quad (4)$$

Figure 3 illustrates this condition, which selects ground pixels depending on the directional sensitivity of the FTIR while
120 keeping the co-location area constant. Here, $\alpha_{90} = 45^\circ$ is selected and r_0 is computed from the radius at a solar zenith angle of 90° , $r_0 = \sqrt{\frac{\alpha_{90}}{360^\circ}} r_{90}$ with $r_{90} = 30$ km. With these selections, the limit of $\vartheta = 90^\circ$ gives the co-location criteria used for the validation of the non-scattering retrieval by Schneider et al. (2020).

Additionally, the time between satellite and ground measurements has to be less than 2 h to minimise representation errors due to the diurnal cycle. Since the FTIR has to directly see the sun (possibly through gaps in the clouds) to take measurements,
125 co-located cloudy satellite observations require a change in the cloud cover within the co-location radius or the co-location time.

At low-altitude stations (i. e. stations below 1000 m above mean sea-level (a. s. l.), only TROPOMI ground pixels with an altitude difference to the station height of less than 500 m are used. If the altitude difference is too large, the observation of different partial columns leads to errors. High-altitude stations are treated separately in Sec. 4.2.



Table 2. List of TCCON ground stations used for the validation.

Station	Latitude	Longitude	Altitude	Data available from/to	Reference
Eureka	80.1° N	86.4° W	610 m	24 Jul 2010–07 Jul 2020	Strong et al. (2019)
Ny Ålesund	78.9° N	11.9° E	20 m	28 Mar 2006–06 Jul 2019	Notholt et al. (2019b)
Sodankylä	67.4° N	26.6° E	190 m	16 May 2009–30 Oct 2019	Kivi et al. (2014)
East Trout Lake	54.4° N	105.0° W	500 m	07 Oct 2016–04 Jul 2020	Wunch et al. (2018)
Bialystok	53.2° N	23.0° E	190 m	01 Mar 2009–01 Oct 2018	Deutscher et al. (2019)
Bremen	53.1° N	8.9° E	30 m	15 Jan 2007–23 Aug 2019	Notholt et al. (2019a)
Karlsruhe	49.1° N	8.4° E	110 m	19 Apr 2010–31 Jul 2020	Hase et al. (2015)
Paris	48.8° N	2.4° E	60 m	23 Sep 2014–23 Jul 2019	Té et al. (2014)
Orléans	48.0° N	2.1° E	130 m	29 Aug 2009–31 Jul 2019	Warneke et al. (2019)
Garmisch	47.5° N	11.1° E	750 m	16 Jul 2007–18 Oct 2019	Sussmann and Rettinger (2018a)
Zugspitze	47.4° N	11.0° E	2960 m	24 Apr 2015–17 Oct 2019	Sussmann and Rettinger (2018b)
Park Falls	45.9° N	90.3° W	440 m	02 Jun 2004–02 Apr 2020	Wennberg et al. (2017)
Rikubetsu	43.5° N	143.8° E	380 m	16 Nov 2013–31 Jul 2019	Morino et al. (2018c)
Lamont	36.6° N	97.5° W	320 m	06 Jul 2008–01 Apr 2020	Wennberg et al. (2016b)
Tsukuba	36.0° N	140.1° E	30 m	04 Aug 2011–31 Jul 2019	Morino et al. (2018a)
Edwards	35.0° N	117.9° W	700 m	20 Jul 2013–04 Jul 2020	Iraci et al. (2016)
JPL	34.2° N	118.2° W	390 m	19 May 2011–14 May 2018	Wennberg et al. (2016a)
Pasadena	34.1° N	118.1° W	240 m	20 Sep 2012–03 Jul 2020	Wennberg et al. (2015)
Saga	33.2° N	130.3° E	10 m	28 Jul 2011–04 May 2020	Kawakami et al. (2014)
Izaña	28.3° N	16.5° W	2370 m	18 May 2007–31 Jul 2020	Blumenstock et al. (2017)
Burgos	18.5° N	120.7° E	40 m	03 Mar 2017–22 Aug 2019	Morino et al. (2018b)
Wollongong	34.4° S	150.9° E	30 m	25 Jun 2008–31 Jul 2019	Griffith et al. (2014)
Lauder	45.0° S	169.7° E	370 m	02 Feb 2010–04 May 2020	Sherlock et al. (2014), Pollard et al. (2019)

130 The effects by different a priori profiles used by FTIR and satellite retrievals are accounted for with the column averaging kernel. Following Borsdorff et al. (2014), the adjustment of column c_i retrieved using prior profile \mathbf{x}_{ai} to prior profile \mathbf{x}_{aj} is performed with the column averaging kernel \mathbf{A}_i of retrieval i by

$$c_s = c_i + (\mathbf{1} - \mathbf{A}_i)^T \mathbf{x}_{aj} \quad (5)$$

135 where $\mathbf{1}$ is a vector of ones. In the present case, i is TROPOMI and j is TCCON. TCCON prior profiles are linearly interpolated from TCCON levels to SICOR layer centres, and the top layer is extended to 0 Pa. This correction is performed for all comparisons with TCCON data except for high-altitude stations.

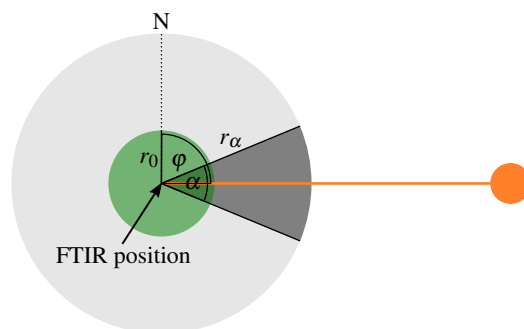


Figure 3. Illustration of the spatial co-location condition. The co-location area consists of a cone in FTIR viewing direction (i. e. solar azimuth angle φ) with opening angle α and radius r_α depending on solar zenith angle ϑ (dark grey). The limit of $\vartheta = 0^\circ$ is a full circle (green). The area remains constant (dark grey and green).

3.2 Ground-based measurements by MUSICA-NDACC

The project MUlti-platform remote Sensing of Isotopologues for investigating the Cycle of Atmospheric water (MUSICA, Schneider et al., 2016; Barthlott et al., 2017) also provides a ground-based water vapour isotopologue data product, which uses spectra measured within the Network for the Detection of Atmospheric Composition Change (NDACC, De Mazière et al., 2018). Two different products exist: firstly the direct retrieval output, called type 1 product, and secondly an a posteriori processed output that reports the optimal estimation of (H_2O , δD) pairs, called type 2 product. Here, the type 2 product is used because it is recommended for isotopologue analyses (Barthlott et al., 2017). Recent MUSICA-NDACC data are currently only available for three stations (Karlsruhe, Kiruna and Izaña), which compromises globally valid validation studies.

Seven stations are in both networks TCCON and NDACC. In these cases, the TCCON and NDACC measurements are performed with the same instrument, but in a different spectral range at different times. As shown e. g. by Schneider et al. (2020), the retrievals from the two networks are biased to each other.

Table 3. List of ground stations used for the derivation of the FTIR correction.

Station	Lat.	Lon.	Altitude	MUSICA available from/to	TCCON available from/to	TCCON reference
Eureka	80° N	86° W	610 m	01 Aug 2006–01 Sep 2014	24 Jul 2010–07 Jul 2020	Strong et al. (2019)
Ny Ålesund	79° N	12° E	20 m	08 Apr 2005–27 Aug 2014	28 Mar 2006–14 May 2018	Notholt et al. (2019b)
Bremen	53° N	9° E	30 m	21 Jul 2004–14 Oct 2014	15 Jan 2007–29 May 2018	Notholt et al. (2019a)
Karlsruhe	49° N	8° E	110 m	17 Apr 2010–12 Sep 2019	19 Apr 2010–25 Jun 2020	Hase et al. (2015)
Izaña	28° N	17° W	2370 m	18 Jun 2001–25 Sep 2019	18 May 2007–30 Jun 2020	Blumenstock et al. (2017)
Wollongong	34° S	151° E	30 m	07 Aug 2007–09 Sep 2014	25 Jun 2008–31 Jul 2019	Griffith et al. (2014)
Lauder	45° S	170° E	370 m	06 Sep 1997–30 Aug 2014	02 Feb 2010–31 Oct 2018	Sherlock et al. (2014)

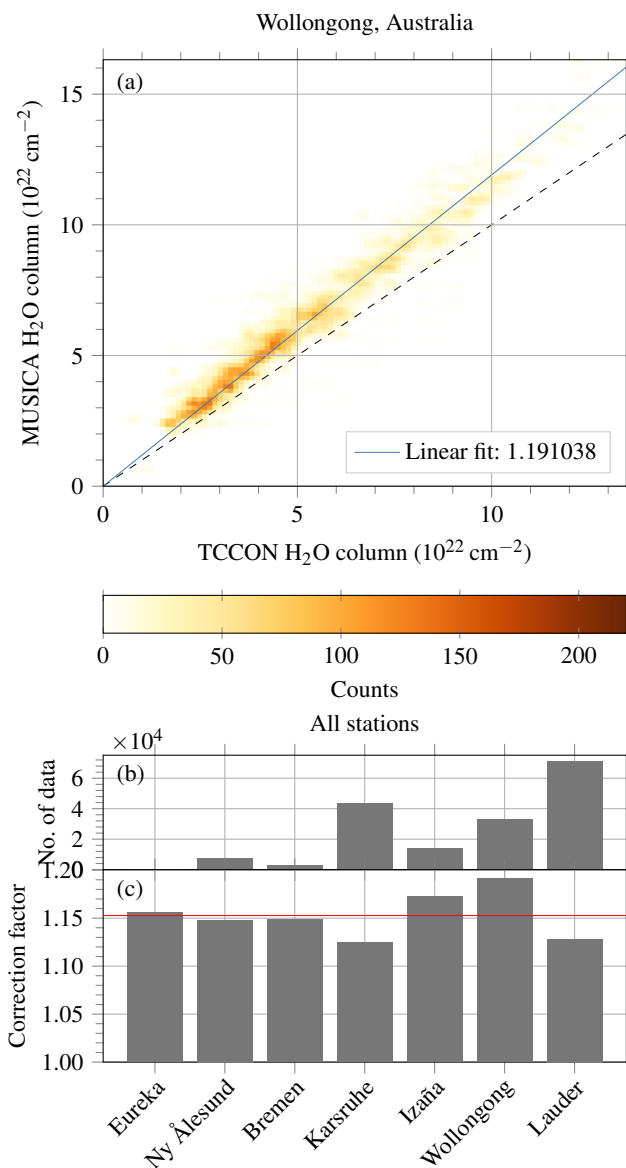


Figure 4. (a) Histogram of co-located TCCON and MUSICA-NDACC H₂O columns at Wollongong (colour-coded) and result of a fit of a linear correction (blue line). (b) Number of co-located observations for all individual stations in both networks. (c) Correction factors to correct MUSICA-NDACC H₂O columns to TCCON. The average 1.1527 is marked by a red line.



Based on the fact that MUSICA δD is calibrated by aircraft measurements near Izaña but TCCON HDO is not verified, Schneider et al. (2020) derived a correction of TCCON HDO by matching TCCON a posteriori δD to MUSICA-NDACC δD .
150 Nevertheless, also H_2O columns differ between TCCON and MUSICA-NDACC. Since TCCON H_2O is better validated and thus assumed to be correct, this discrepancy is solved by a correction of MUSICA-NDACC derived below. Figure 4a shows correlations of TCCON and MUSICA-NDACC H_2O columns at Wollongong, Australia. The difference is well described by a simple scaling of the column. The result of such a fit for all stations in both networks (as listed in Tab. 3) is presented in Fig. 4c. The correction factors do not vary considerably between stations. To harmonise both data sets, MUSICA H_2O
155 and HDO columns are thus corrected by division by the mean correction factor 1.1525 (red line in Fig. 4c). This adjusts the MUSICA H_2O columns while leaving MUSICA δD unchanged.

Filling the null-space of TROPOMI measurements with MUSICA-NDACC prior profiles with averaging kernels creates large scatter and deviations from the reference. MUSICA a priori profiles do not depend on time and are much less realistic than TCCON or TROPOMI prior profiles. This can lead to deviations. Thus, averaging kernels are not applied for the validation
160 with MUSICA-NDACC data.

3.3 Aircraft measurements by the WISPER instrument

During the NASA ObseRvations of Aerosols above CLouds and their intEractionS (ORACLES) field mission in the south-eastern Atlantic Ocean region (Redemann et al., 2021), measurements of H_2O mixing ratio and δD were taken onboard the NASA P-3B Orion aircraft with the Water Isotope System for Precipitation and Entrainment Research (WISPER) instrument
165 (Henze et al., 2021). This instrument employs in situ gas phase cavity ring-down water vapour isotopic analysers (Picarro model L2120-fi) coupled to inlets that enable paired measurements of cloud water and total water amounts and isotope ratios..

The validation uses profile measurement data from the 2018 deployment. Only profiles reaching at least 5000 m are taken into account. For ascent profiles, descending sections are filtered out by discarding sections with higher pressure than a previous data point; similarly, ascending sections are removed from descent profiles. If more than 30 % of the data are discarded in this
170 step, the whole profile is dropped. This eliminates flight sections with a “saw-tooth” pattern designed for sampling in cloudy regions. Altogether, 17 profiles pass the filter, spanning the time range from 27 Sep 2018 to 21 Oct 2018. The top altitude varies between 5130 m and 7408 m with an average of 6195 m. The vertical resolution is typically 30 m due to sampling at 1 Hz and typical aircraft decent rates. HDO mixing ratios are computed from H_2O mixing ratios and δD . In order to compute a total column corresponding to the profile, each measured mixing ratio is assumed to be constant until the data point below,
175 with the lowest measurement assumed constant down to the surface with surface pressure taken from the ECMWF analysis data product interpolated to the location of the profile.

The co-location is performed with the full 360° viewing angle (as the in situ instrument does not have a directional sensitivity like the FTIR) and a radius of 10.6066 km (corresponding to the radius for the full circle r_0 in Sec. 3.1). For each co-located measurement, the satellite prior profile is scaled such that the partial column below the ceiling of the aircraft profile coincides
180 that of the aircraft measurement. The aircraft profile is interpolated to the grid of the prior profile, and the part above the ceiling is complemented by the upper part of the scaled prior profile. Finally, the averaging kernel A_i of the satellite measurement is



applied to compute the smoothed reference column by

$$x_{\text{ref},s} = \mathbf{A}_i^T \mathbf{x}_{\text{ref}}. \quad (6)$$

4 Validation

185 In the following subsections, the scattering retrieval is validated for clear-sky and cloudy scenes according to retrieved effective cloud parameters as described above in Sec 2. As reference, the plots additionally show the non-scattering retrieval filtered as reported by Schneider et al. (2020), i. e. with the cloud fraction from the Visible Infrared Imaging Radiometer Suite (VIIRS) co-located to the TROPOMI field of view, a two-band filter as described in loc. cit., and by solar zenith angle.

4.1 Low-altitude stations

190 Figure 5 depicts an exemplary time series of daily medians of co-located measurements at the TCCON station Karlsruhe. The TROPOMI observations follow the reference well, although some deviations are present especially for cloudy scenes. Figure 6 presents corresponding correlations. Retrieved columns correlate excellently to the reference with a Pearson coefficient of 0.98 in H_2O and 0.99 in HDO for clear-sky scenes, and 0.95 in H_2O and 0.96 in HDO for cloudy scenes. A posteriori δD has more scatter with correlation coefficients of 0.86 and 0.83 for clear-sky and cloudy scenes, respectively. The bias, which is defined
195 as the mean difference between TROPOMI and TCCON, is for clear-sky scenes $-1.3 \times 10^{20} \text{ molec cm}^{-2}$ (-0.4%) in H_2O and $-3.6 \times 10^{16} \text{ molec cm}^{-2}$ (-1.0%) in HDO, which corresponds to a bias in a posteriori δD of -3% (1.1%). For cloudy scenes, it is $4.9 \times 10^{21} \text{ molec cm}^{-2}$ (8.3%) in H_2O , $1.1 \times 10^{18} \text{ molec cm}^{-2}$ (6.5%) in HDO and -12% (7.3%) in a posteriori δD . The retrieval performance for cloudy scenes is good: correlations are similar as for clear-sky scenes or the non-scattering retrieval, although the bias is larger. This can be explained by small sensitivity of the retrieval below optically thick clouds.

200 Figure 7 presents statistics and correlation coefficients of daily medians at all low-altitude stations. The amount of data for clear-sky scenes of the new scattering retrieval is much larger than for the old non-scattering retrieval: on average a factor of 8 more. This is connected to different filtering: while the non-scattering product is strictly filtered with the S5P-VIIRS product and an additional two-band filter (Schneider et al., 2020), the scattering product is filtered with effective cloud parameters retrieved in the pre-fit (see Table 1). The number of observations (ground pixels) per day (Fig. 7b) is usually around 4 but
205 significantly higher at high latitudes due to multiple overpasses per day. Cloudy scenes encounter typically less observations per day compared to clear-sky scenes with a median of 3.4 vs. 4.1. The non-scattering retrieval has a significantly lower data yield with a median of 2.7 co-located ground pixels per day. The distributions visualised by the violin plots show that there is quite some spread with some days with a high number of observations.

Correlations of daily medians of H_2O and HDO columns are excellent at all stations (Fig. 7c, d). In a posteriori δD , correlations are lower at some stations, typically ones with low seasonal variation (Fig. 7e). For clear-sky scenes, correlation
210 coefficients are similar to those of the non-scattering product except for δD at some stations like JPL and Pasadena. For cloudy scenes, the correlations are mostly slightly lower than for clear-sky scenes.

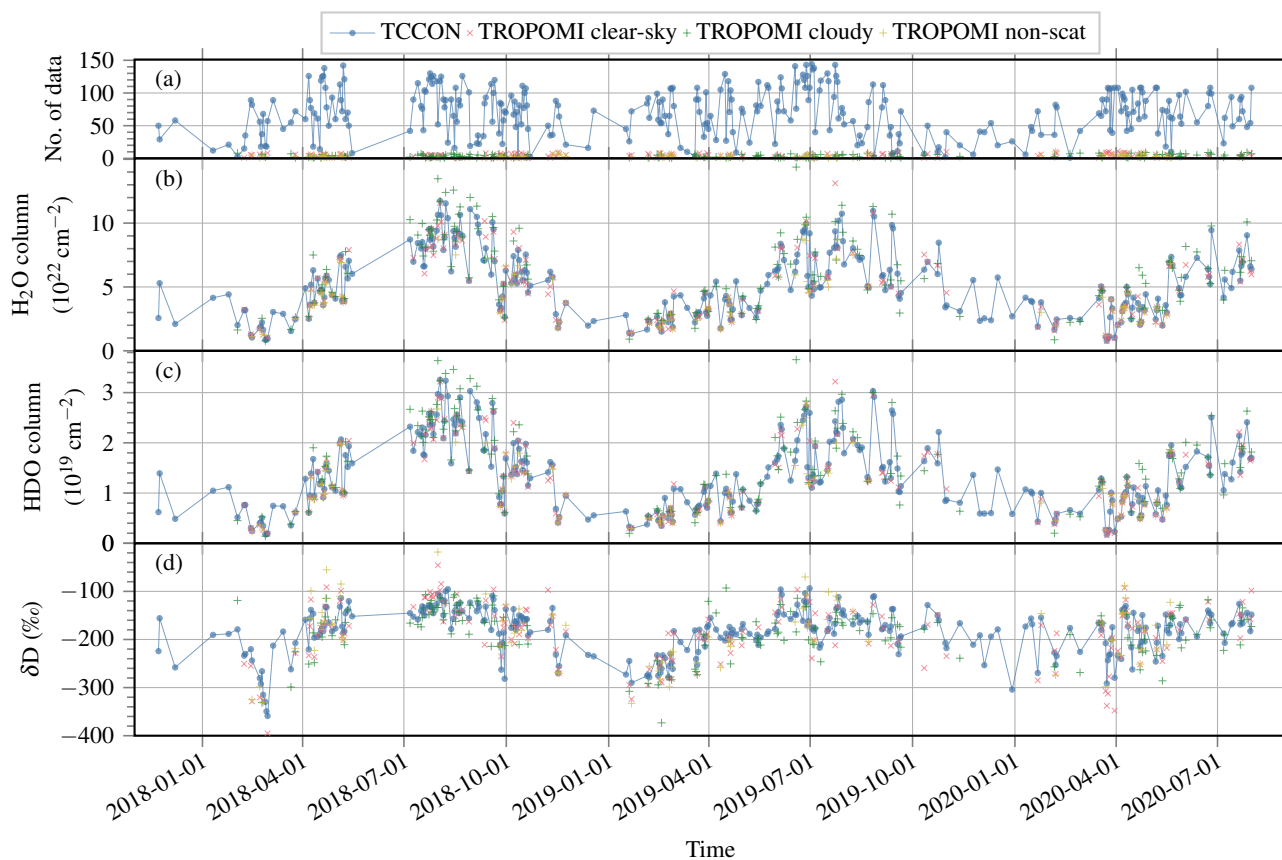


Figure 5. Time series of individual observations per day (a), daily medians of H₂O columns (b), HDO columns (c) and a posteriori δD (d) of TCCON (blue), TROPOMI clear-sky scenes (red), TROPOMI cloudy scenes (green), and the TROPOMI non-scattering retrieval (orange) at Karlsruhe, Germany (49.1° N, 8.4° E, 110 m a. s. l.)

Biases are depicted in Fig. 8. At low and middle latitudes the bias is generally small: at these stations, the median for clear-sky scenes is 1.3×10^{21} molec cm⁻² (1.8 %) in H₂O columns, 2.0×10^{16} molec cm⁻² (−0.3 %) in HDO columns, and −8 ‰ (4.6 %) in δD , the one for cloudy scenes is 4.7×10^{21} molec cm⁻² (8.8 %) in H₂O columns, 1.1×10^{18} molec cm⁻² (6.5 %) in HDO columns, and −20 ‰ (12 %) in δD . High-latitude stations mostly have larger biases that can be as high as 20 % in the columns and 40 ‰ in a posteriori δD . The median bias at high latitude stations (Eureka, Ny Ålesund, Sodankylä, and East Trout Lake) in H₂O, HDO and δD is for clear-sky scenes 2.3×10^{21} molec cm⁻² (9.5 %), 4.0×10^{17} molec cm⁻² (0.4 %) and −37 ‰ (13 %) and for cloudy scenes 5.1×10^{21} molec cm⁻² (12 %), 1.0×10^{18} molec cm⁻² (9.1 %) and −24 ‰ (8.4 %), respectively. These high biases are similar, but partly more pronounced than for the non-scattering retrieval. High-latitude locations employ difficult measurement geometries with typically high solar zenith angles and low surface albedos, in which the additional estimation of cloud parameters seems to be even more challenging. In summer, these biases are typically lower than in darker seasons with higher solar zenith angles. The bias is also high at Garmisch, which lies in a mountainous region

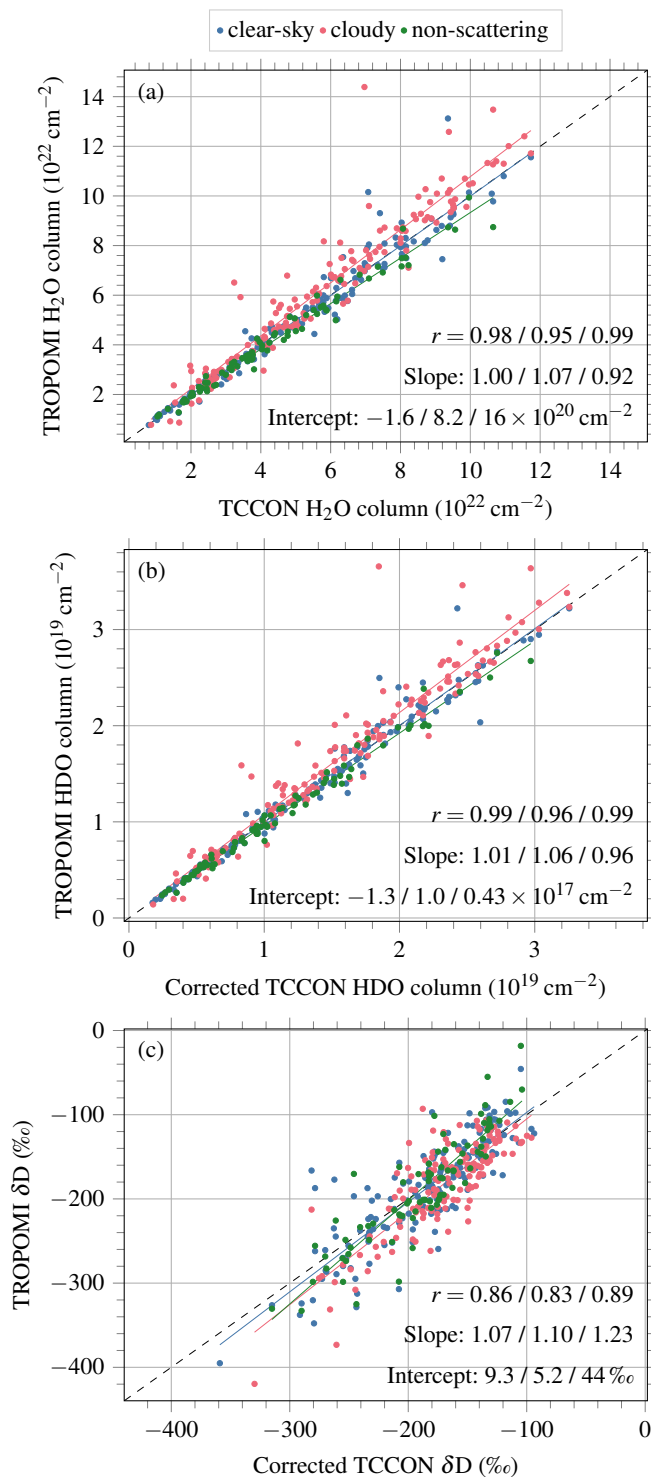


Figure 6. Correlations of TROPOMI observations against corrected TCCON measurements of H₂O columns (a), HDO columns (b) and a posteriori δD (c) at Karlsruhe.

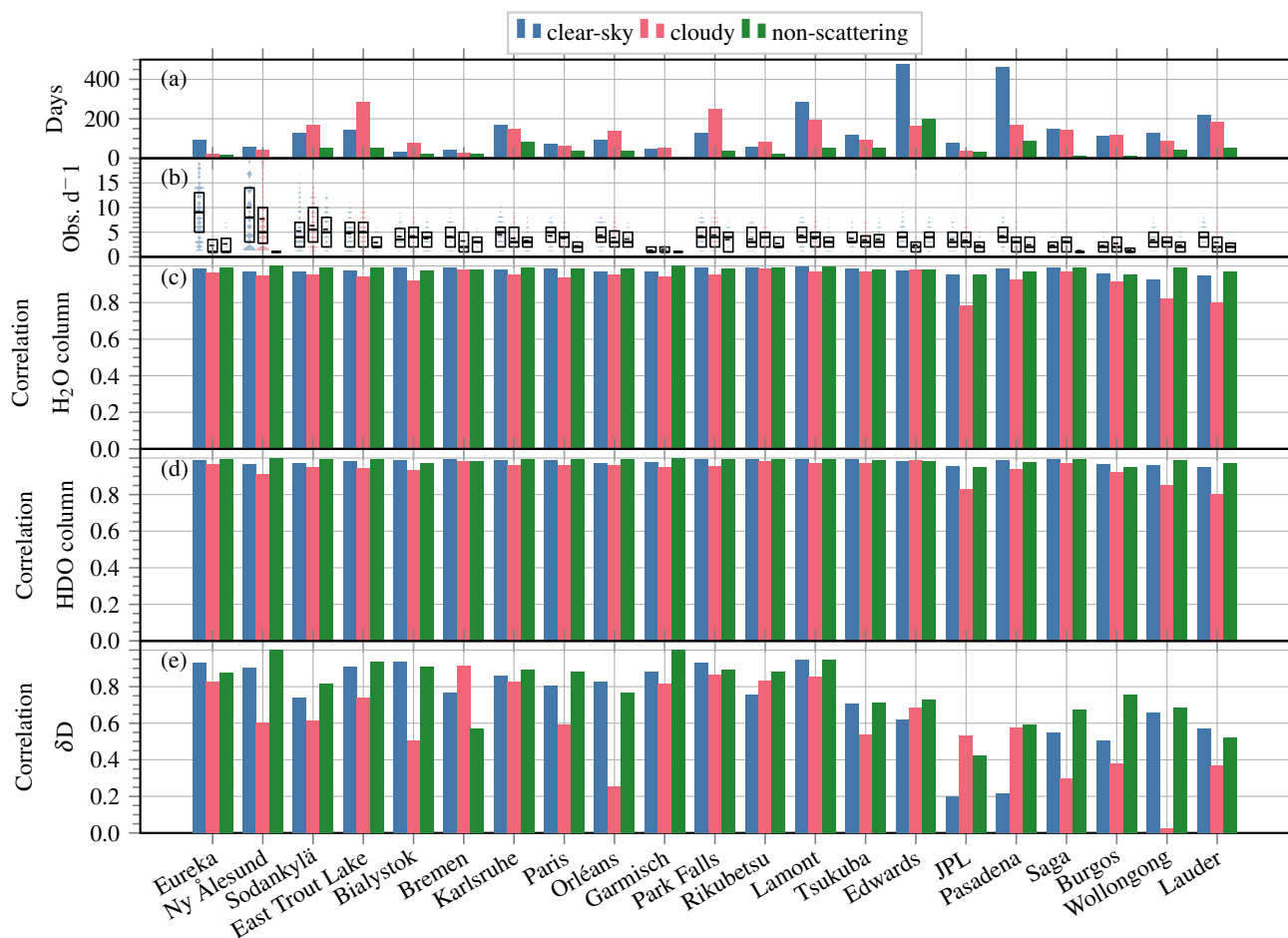


Figure 7. Number of days with observations (a), observations per day (b), correlation coefficients of H₂O columns (c), correlation coefficients of HDO columns (d), and correlation coefficients of a posteriori δD (e) at all TCCON stations.

meaning a typically complex topography with large variation in surface altitude and albedo within a ground pixel. The median bias of all stations is for clear-sky scenes 1.4×10^{21} molec cm⁻² (2.9 %) in H₂O columns, 1.1×10^{17} molec cm⁻² (-0.3 %) in HDO columns, and -17‰ (9.9 %) in a posteriori δD . For cloudy scenes, it is 4.9×10^{21} molec cm⁻² (11 %) in H₂O, 1.1×10^{17} molec cm⁻² (7.9 %) in HDO, and -20‰ (9.7 %) in a posteriori δD . Although the absolute bias in δD is higher for cloudy scenes than for clear-sky scenes, the relative bias is not. This is connected to different conditions in cloudy and clear-sky weather. The distributions of the differences (TROPOMI – TCCON, visualised by the violin plots in Fig. 8) vary considerably between stations. Outliers are present, which shows that statistics over an adequate amount of data is needed for interpretation. Altogether, the performance of the new scattering retrieval for clear-sky scenes is similar to the one of the non-scattering retrieval, even though the scattering retrieval yields much more data. Biases are slightly smaller in HDO but slightly larger in a posteriori δD .

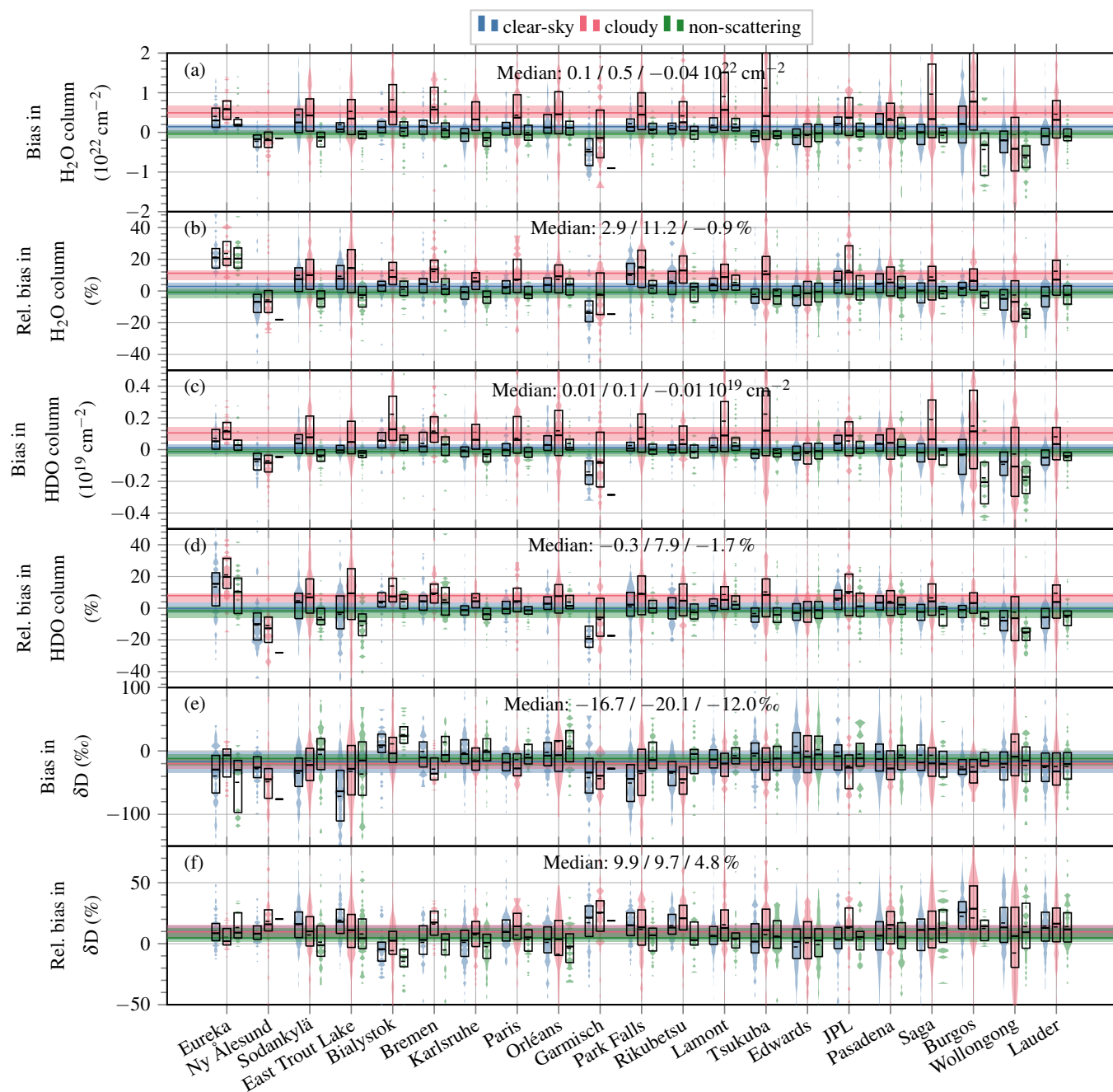


Figure 8. Bias in H₂O columns (a), relative bias in H₂O columns (b), bias in HDO columns (c), relative bias in HDO columns (d), bias in δD (e), relative bias in δD (f) for clear-sky scenes (blue), cloudy scenes (red) and the non-scattering retrieval (green). The violin plots visualise the distributions of differences between TROPOMI and TCCON, the boxplots mark quartiles and the dashed lines inside the boxes the mean. Coloured horizontal lines denote station-to-station medians and the shading around them the station-to-station quartiles.



For a direct comparison of the new scattering retrieval to the non-scattering retrieval by Schneider et al. (2020), only
235 ground pixels for which both retrievals yield valid data are considered. The distributions of the differences (TROPOMI –
TCCON) is very similar at most stations, with significant differences only at the coastal stations Burgos and Wollongong
and at Park Falls. The station-to-station median bias for this scene selection at low and middle latitude stations is in H₂O
 4.4×10^{20} molec cm⁻² or 0.3 % for the scattering retrieval vs. -4.2×10^{18} molec cm⁻² or 0.4 % for the non-scattering retrieval
and in HDO -4.5×10^{16} molec cm⁻² or -1.1 % vs. -9.3×10^{16} molec cm⁻² or -1.3 %. In a posteriori δD it is -14‰ (7.5 %)
240 for the scattering retrieval vs. -11‰ (5.4 %) for the non-scattering retrieval. This demonstrates that the performance of both
retrievals is comparable.

4.2 High-altitude stations

Ground stations on high mountains are special because the station height and the mean surface altitude of co-located satellite
ground pixels typically differ considerably, which means that different air columns are observed by both. This leads to high
245 biases if not accounted for. Therefore, the chosen prior plays an important role in this situation. To demonstrate the role of the
prior in potential corrections, an additional run with HDO prior profiles obtained by an assumed more realistic δD profile as
described in Sec. 2 has been performed. During the co-location, the same ground pixels are considered for both runs. Moreover,
averaging kernels are not applied for this analysis because the prior profiles of the retrieval are used for the altitude correction.

The left column of Fig. 9 demonstrates the high biases of uncorrected clear-sky observations near Zugspitze (2964 m a. s. l.),
250 which for the standard prior amount to 185 % in H₂O, 232 % in HDO and 75‰ in δD . Nevertheless, the time series does
follow the relative variability of the reference.

The ground station on top of the mountain is always higher than the (mean) ground pixel altitude. To correct for the altitude
differences, the partial columns of the TROPOMI observations above the station height are considered by truncating the scaled
profile of the retrieval at the altitude of the station. This is the same procedure applied by Schneider et al. (2018, Sec. 4). The
255 second column of Fig. 9 depicts the resulting time series. The bias in both H₂O and HDO is greatly reduced to -54 % and
-48 % for the standard prior and -55 % and -54 % for the depleted prior. In a posteriori δD a large difference between both
priors is visible: while the bias for the scaled prior is practically the same as for the uncorrected case, 73‰, it is largely reduced
to 4‰ for the depleted prior. The first is due to the fact that the altitude correction in H₂O and HDO cancels out when dividing
HDO by H₂O if the same profile shapes are used. On the other hand, the small bias in δD in the second case shows that the
260 assumed depleted HDO profile shape is indeed a good estimate for this case.

Another possibility is to utilise the shielding of clouds. To this end, scenes with optically thick clouds at an altitude similar
to the station height as specified in Tab. 4 are selected. In these cases, the satellite measurement is sensitive above the cloud
but insensitive below the cloud. Figure 10 illustrates the corresponding averaging kernels for a clear-sky and a cloudy scene.
Since the FTIR has to see the sun and thus can measure only through gaps in the clouds or when the cloud cover changes
265 within the co-location time, the amount of data for cloudy scenes is very small. Thus, the co-location radius is extended to
 $r_{90^\circ} = 50$ km in this case. The inferred columns are corrected for the altitude difference between ground pixel and station height
as described above. The right panel of Fig. 9 depicts the resulting time series. The biases in the columns and in a posteriori δD

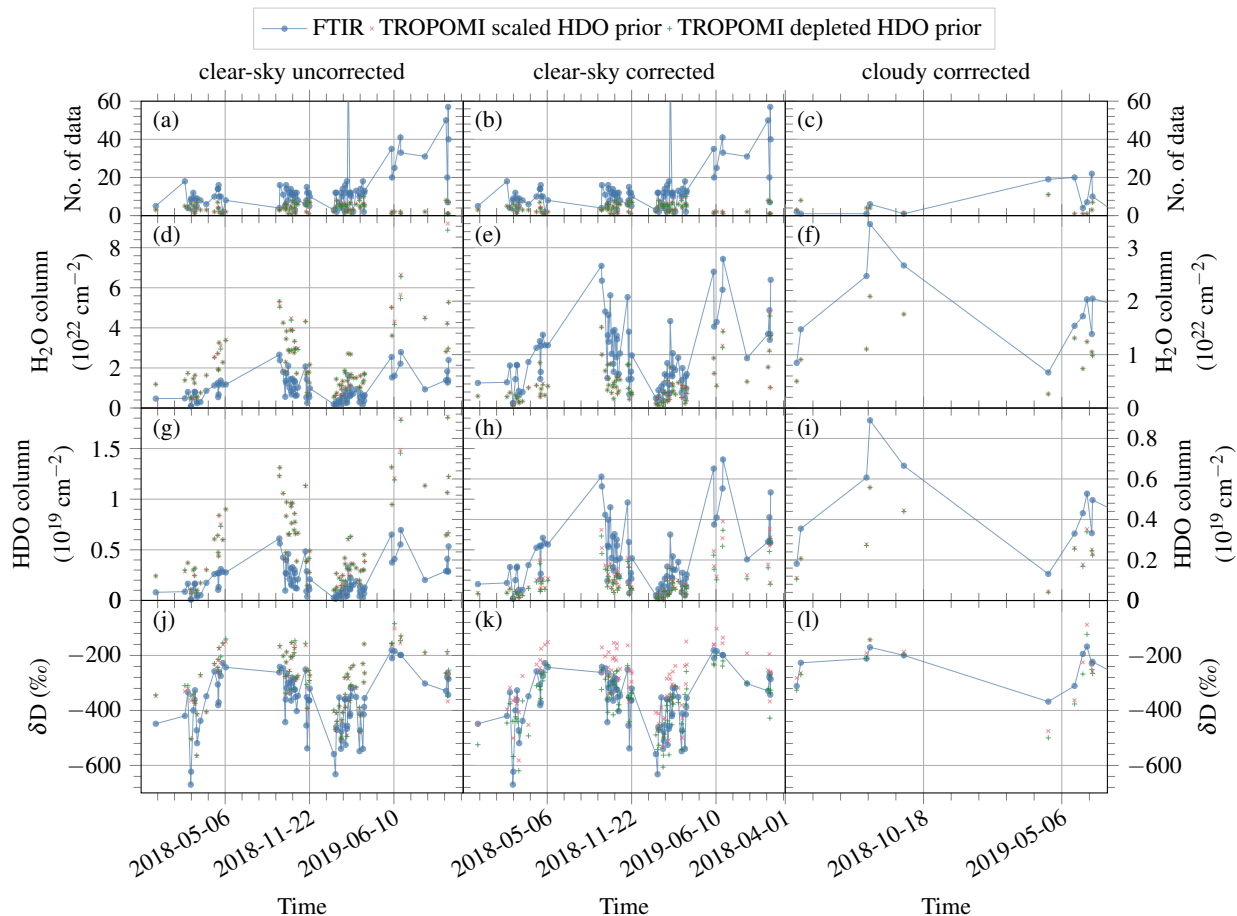


Figure 9. Time series of the amount of individual measurements per day near (first row), bias in H₂O column (second row), bias in HDO column (third row), and bias in δD (fourth row) at the high-altitude station Zugspitze (2964 m a. s. l.). The left panels (a), (d), (g) and (j) show clear-sky measurements without altitude correction; the centre panels (b), (e), (h) and (k) show the same measurements with altitude correction; and the right panels (c), (f), (i) and (l) show observations over optically thick clouds within an altitude range 1000 m above and 500 m below the station height. Please note that in the left panels the H₂O and HDO axes are different than in the centre and right panels, as indicated by the axis ticks.

Table 4. Filter criteria for cloudy-sky scenes at high-altitude stations. Here h_s denotes the height of the ground site.

Quantity	Filter
Filter for cloudy scenes	
Cloud height	$h_s - 500\text{m} \leq h_{\text{cld}} \leq h_s + 1000\text{m}$
Cloud optical thickness	$\tau_{\text{cld}} \geq 2$

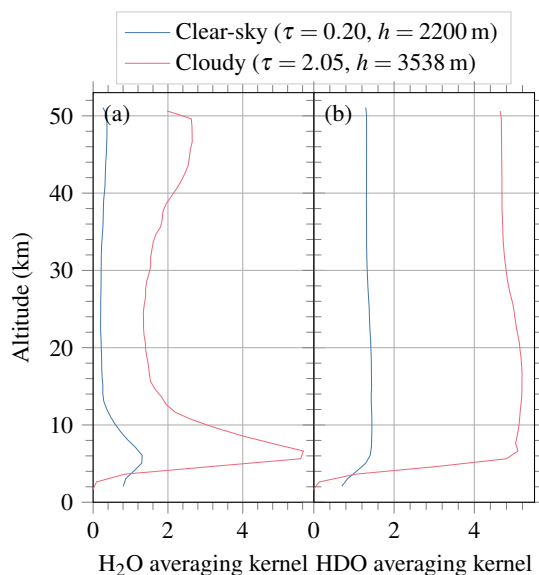


Figure 10. Averaging kernels of H₂O (a) and HDO (b) for a clear-sky scene (orbit 4725 on 11 Sep 2018, blue) and a cloudy scene (orbit 4839 on 19 Sep 2018, red) near Zugspitze.

are acceptable for both priors. They amount to 4‰ for the scaled prior and −24‰ for the depleted prior. That the shielding yields good agreement with the scaled prior shows that the data provides information about the vertical distribution.

270 Figure 11 depicts biases for both high-altitude stations Zugspitze and Izaña. It confirms the behaviour seen in the time series at Zugspitze for both stations. Uncorrected clear-sky observations yield a large bias in all quantities. The altitude correction greatly reduces the bias in the H₂O and HDO columns. In δD , the correction cancels out when assuming the same vertical distributions of H₂O and HDO so that the bias remains. However, the altitude correction with a realistic prior yields a substantial reduction of the bias in δD . For cloudy scenes with optically thick clouds in similar altitudes than the station height, the biases
275 are also relatively small, although the validation is hampered by a small amount of data.

4.3 MUSICA-NDACC

Recent MUSICA-NDACC data are available for two low-altitude stations. Karlsruhe is also in the TCCON network so that a comparison is possible. MUSICA-NDACC provides fewer measurements than TCCON (113 vs. 170 for clear-sky scenes and 83 vs. 148 for cloudy scenes). This is, among others, due to longer duration of individual FTIR measurements for NDACC
280 compared to TCCON. Correlations, as shown in Figure 12, are excellent in the retrieved columns. For clear-sky scenes, Pearson coefficients are 0.98 in H₂O and 0.99 in HDO, the same numbers as for TCCON (compare Fig. 6). For cloudy scenes, correlations with MUSICA-NDACC are with 0.98 in H₂O and 0.99 in HDO even better than with TCCON, however with considerably less data points. A posteriori δD also has excellent correlation coefficients of 0.93 for clear-sky scenes and 0.91 for cloudy scenes, which is better than with TCCON. The bias for clear-sky scenes is $1.8 \cdot 10^{21}$ molec cm^{−2} (2 %) in H₂O,

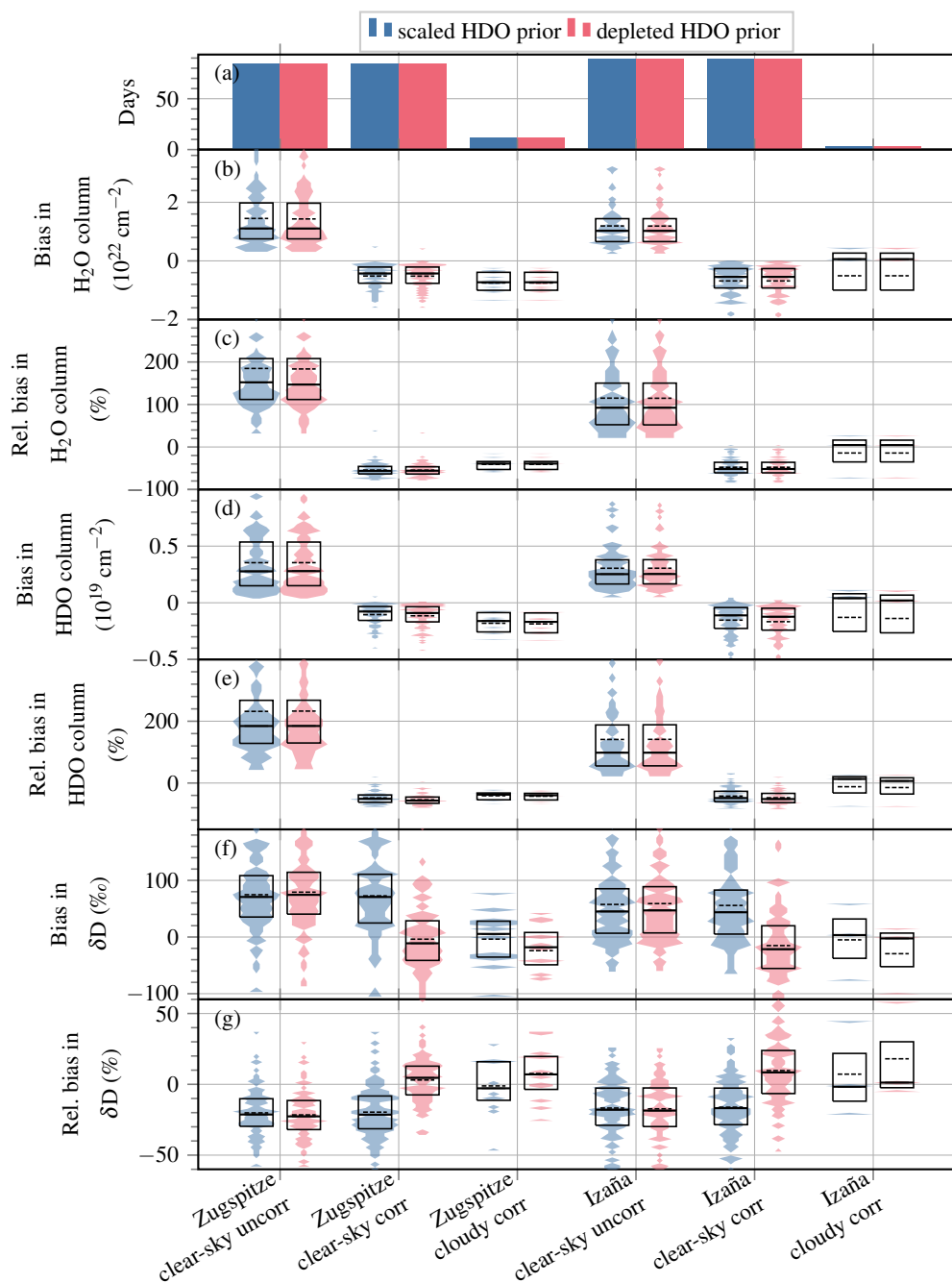


Figure 11. Biases for high-altitude TCCON stations plotted similarly as in Fig. 8, but for retrievals with the standard scaled HDO prior profile (blue) and a HDO prior profile obtained by assuming a more realistic δD profile described in Sec. 2. Shown are (a) the number of days with observations, (b) the bias in H_2O columns, (c) the relative bias in H_2O columns, (d) the bias in HDO columns, (e) the relative bias in HDO columns, (f) the bias in δD , and (g) the relative bias in δD . For each station, three entries are shown which correspond to uncorrected clear-sky observations, clear-sky observations corrected for the station altitude and altitude-corrected cloudy observations.

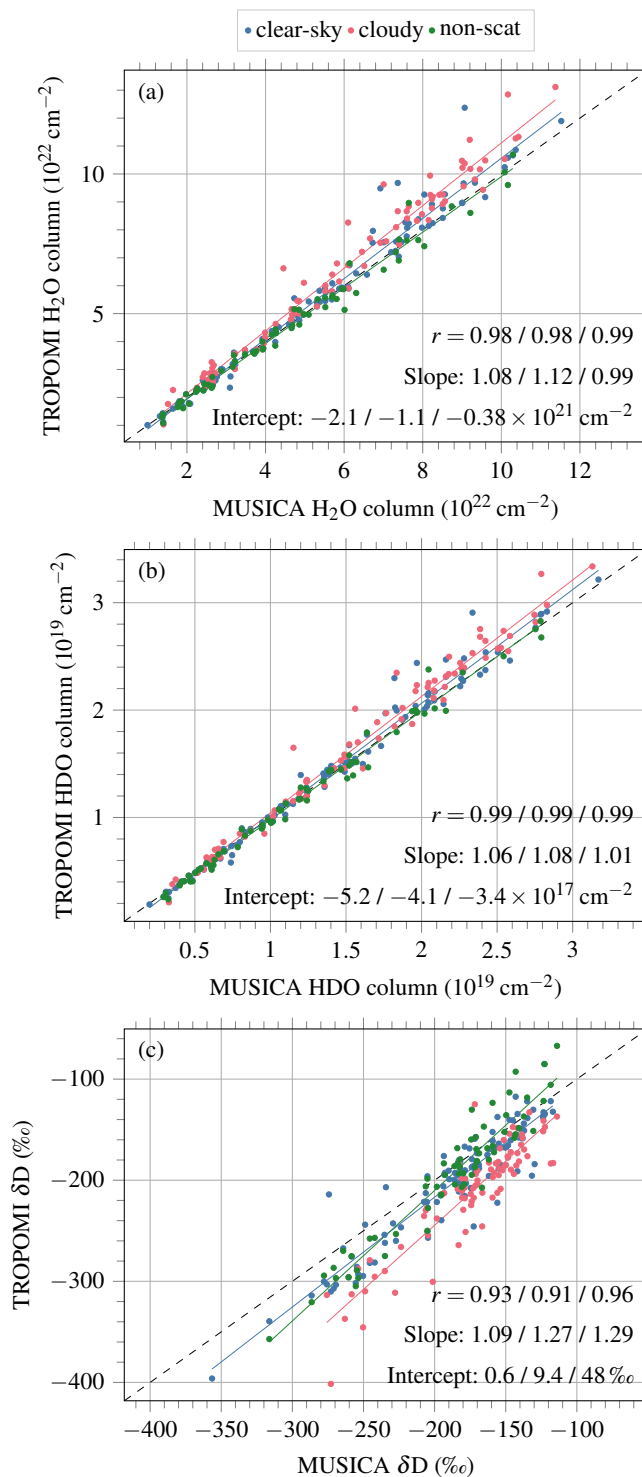


Figure 12. Correlations of TROPOMI observations against corrected MUSICA-NDACC measurements of H₂O columns (a), HDO columns (b) and a posteriori δD (c) at Karlsruhe.



285 2.5×10^{17} molec cm⁻² (-0.1 %) in HDO, and -16‰ (8.4 %) in δD . For cloudy scenes, the bias is 6.4×10^{21} molec cm⁻²
(9.9 %) in H₂O, 9.3×10^{17} molec cm⁻² (4.8 %) in HDO, and -37‰ (21 %) in δD . This is significantly larger than for TCCON.

Only one other low-altitude station provides MUSICA-NDACC data with temporal overlap with the TROPOMI mission,
namely Kiruna. This is a high-latitude station, so that high biases are expected. They amount to $2.6 \cdot 10^{21}$ molec cm⁻² (4.6 %)
in H₂O, $1.6 \cdot 10^{17}$ molec cm⁻² (-3.5 %) in HDO, and -58‰ (24 %) in δD for clear-sky scenes and $5.0 \cdot 10^{21}$ molec cm⁻²
290 (12 %) in H₂O, $6.4 \cdot 10^{17}$ molec cm⁻² (5.1 %) in HDO, and -51‰ (23 %) in δD for cloudy scenes. With only two stations, it
is not meaningful to make statistical statements.

4.4 WISPER aircraft measurements over the ocean

In order to validate the retrievals over oceans, aircraft profiles from the ORACLES field campaign in 2018 are used as reference.
The data reduction method is described in Sec. 3.3.

295 Figure 13 shows a time series of total columns computed from aircraft profiles and co-located TROPOMI retrievals over
the North Atlantic ocean. The bias is $(-6.1 \pm 11) \times 10^{21}$ molec cm⁻² or (-3.9 ± 6.9) % in H₂O and (-3 ± 15) ‰ in δD . The
validation over the ocean is hampered by very few data points. Nevertheless, the comparison to the aircraft profiles shows that
the performance of the retrieval over the ocean is good.

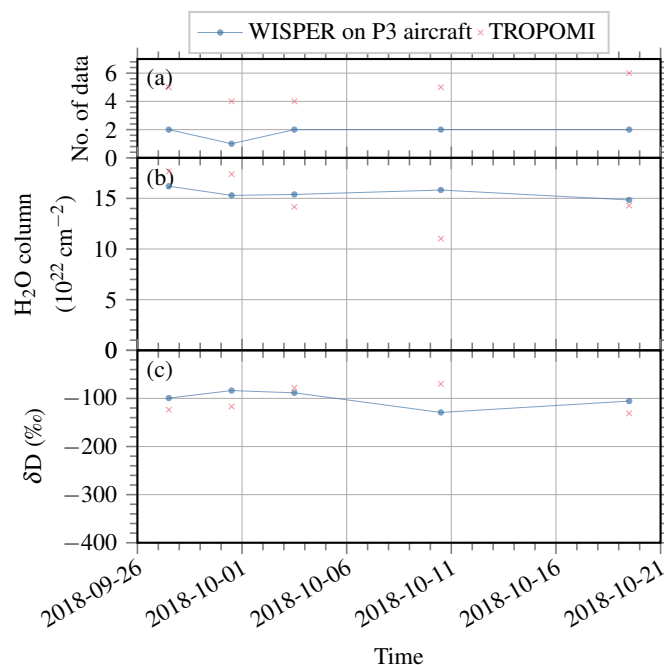


Figure 13. Times series of (a) number of measurements, (b) daily averaged total columns of H₂O and (c) δD from aircraft profiles (blue) and co-located TROPOMI retrievals (red).

5 Demonstration of applications of the data set

300 5.1 Global picture

Figure 14 demonstrates a global picture of the new data set with a monthly average for September 2018. The most prominent improvement compared to the plot of the non-scattering product shown in Schneider et al. (2020, Fig. 10) is a huge enhancement

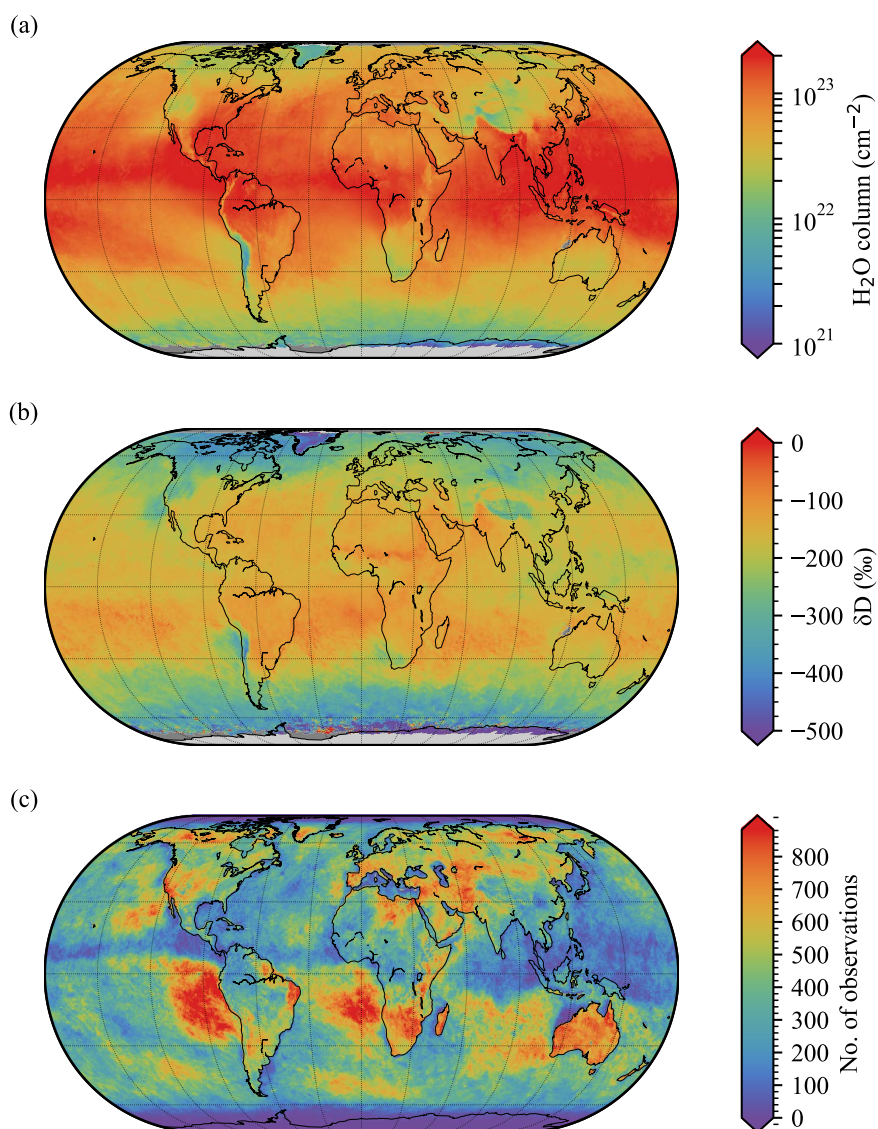


Figure 14. Global plots of (a) average H_2O , (b) average δD , and (c) number of observations for September 2018 on a $0.5^\circ \times 0.5^\circ$ grid. The average of δD is weighted with the H_2O column.



in data coverage, most prominently over the oceans and in regions at low latitudes with persistent clouds (e. g. over the Amazon, Central Africa and Oceania), where the non-scattering retrieval yields no data. Near these regions and also over northern India, δD is lower than in the clear-sky only data product which is attributed to different weather conditions at cloudy days compared to clear-sky days.

In the spatial distribution of column integrated H_2O and δD shown in Fig. 14 the major characteristic features of the atmospheric water cycle and the isotopic effects as described by Dansgaard (1964) can be recognised. In Fig. 14a, a very moist intertropical band can be distinguished. The typically deep convective clouds associated with the moistest band shield most of the scenes in the area of the intertropical convergence zone (Equatorial Atlantic, and Pacific, see Fig. 14c). This might lead to a slight underestimation of the total column δD in this area. The moist continental regions associated with the northern hemisphere's fading summer monsoon systems (West African Monsoon, southeast Asian Monsoon) show relatively more depleted δD total columns (see coastal West Africa, China) compared to other regions in the same latitudinal band (see subtropical oceans, India and North Africa). The combined (H_2O , δD) information is likely to provide more insight into mixing and cloud and below cloud evaporation effects in these regions (Noone, 2012).

The subtropical ocean regions are all associated with relatively high total column δD except for spots with distinctly lower values found along the eastern coasts of the ocean basins. In the latter coastal regions around 30° N/S stratocumulus capped areas with strong inversions are prominent and enhanced subsidence is frequently observed (Norris, 1998; Myers and Norris, 2013), which probably leads to the distinct local minima in total column δD and total column H_2O .

In the regions of frequent occurrence of extratropical cyclones (storm tracks) over the midlatitude western North Atlantic, western North Pacific and in the Southern Ocean, sharp gradients can be observed in total column δD . The equatorward flanks of the storm tracks are associated with warm air and total column δD of about -100‰ . In contrast, much lower values of about -300‰ can be observed on the subpolar flanks of the storm tracks. In these regions the frequent occurrence of extratropical cyclones (Wernli and Schwierz, 2006) strongly modulate the variability of δD signals of atmospheric water vapour (Thurnherr et al., 2020b). In the Southern Ocean, the spatial pattern of oceanic total column δD reflects the spiral shaped winding of the Southern Ocean storm track around Antarctica with more frequent storms in the central South Atlantic compared to the Central South Pacific. In the latter region a tongue of more enriched total column δD reaches far south towards the Antarctic coast.

Along the Antarctic coast, the very low total column δD might be due to cold air outbreaks or strong katabatic outflows at low levels, advecting very depleted Antarctic water vapour over the ocean (Thurnherr et al., 2020b). However, the data availability over these coastal Antarctic region is very limited (Fig. 14c). A comparison with high resolution isotope-enabled numerical model simulations in these regions as well as in very high altitude mountainous regions, would certainly help in ruling out important biases due to uncertainties associated with the retrieval in these regions with complex topography and small-scale variations in the albedo.

The data coverage, as can be seen on the example for the month of September 2018 in Fig. 14c, is highly variable in space. Particularly over tropical oceanic regions, the data is very sparse due to shielding by high clouds. Over high latitude land regions, the data is also sparse due to high solar zenith angles and low surface albedos (recall the SZA filter and albedo filter,



cf. Tab. 1). In contrast, particularly in regions of enhanced subsidence in the subtropics a large number of observations are available. A weak seasonal cycle in the amount of observations exists particularly at high latitudes.

5.2 Single overpasses

340 Figure 15 demonstrates single overpass results over the North Atlantic Ocean. On 17 January 2020 a cold air outbreak forms along the North American east coast, behind a cold front associated with a North Atlantic cyclone. The cold front can be identified in Fig. 15a by the quasi-zonal cloudy band, marked by a strong gradient of low to high total column H_2O between 15°N and 25°N across the front. The cold air mass (see low values of potential temperature at 850 hPa behind the cold front in Fig. 15f) travels southward towards the tropics between 17 and 20 January 2020 (Figs. 15–17). The cold, subsiding air behind
345 the cold front is very dry (Fig. 15a) and is associated with low total column δD values between -400 and -200‰ (Fig. 15b) which are characteristic of the cold sector of extratropical cyclones (Thurnherr et al., 2020a). Marine cold air outbreak clouds are typically low level clouds with high cloud fraction (stratocumulus, cumulus, Fig. 15e) and moderate optical thickness (Fig. 15c, Fletcher et al., 2016). The very high δD values of $\sim 0\text{‰}$ stretching in a bow from $\sim 20^\circ \text{N}$, 40°W westward are caused by low sensitivity in low altitudes due to cloud shielding. These sensitivity issues are reflected by very low values of the
350 column averaging kernel (Fig. 15d). The magnitude of the null-space error is determined by the deviation of the shape of the prior profile to the real profile. The prior depends on time and location, thus the null-space error may be different in different regions. Nevertheless, these data still contain valuable information that can be interpreted in combination with measurements or model simulations providing vertical profiles of H_2O and HDO that can be combined with the vertical sensitivity of the satellite retrievals.

355 The analysis of successive overpasses between 18 and 20 January (Fig. 16, 15, 17) shows a rapid moistening of the originally very dry and depleted cold air mass. When it leaves the North American continent on 18 January the cold sector air has total column δD of less than -400‰ . On 20 January, when the cold front reaches into the tropics, the δD of the cold sector is in the range -300 to -200‰ . The dry and cold air subsiding above the boundary layer typically induces large humidity gradients near the ocean surface and consequently leads to enhanced surface evaporation fluxes that favour a rapid moistening
360 and continuous increase in δD of cold sector air as it travels southward (Aemisegger and Papritz, 2018). The δD in Fig. 15b shows large spatial variability in the cold sector hinting towards different degrees of vertical mixing in different regions of the cold sector, most likely due to variations in subsidence strength. The latter aspect could be investigated in more detail using this dataset in combination with a numerical weather model including isotopes.

This variability in δD at low total column H_2O can also be observed when displaying the cold sector data in a (H_2O , δD)
365 phase space (Fig. 18). In contrast to the cold air mass behind the cold front, the trade wind air mass in front of the cold front is associated with very high total column δD (Fig. 18b). Reduced subsidence and stronger shallow convective activity with deeper clouds are the reason for the higher δD on the warm, trade wind side of the front (see also Aemisegger et al., 2020, for a discussion on the impact of extratropical intrusions behind cold fronts on the low-level δD signals in the tropics).

In future comparisons of TROPOMI all-sky observations with vertical profiles from aircraft-based measurement campaigns
370 will be helpful for identifying potentially remaining biases in very dry compared to very moist conditions. Furthermore, studies

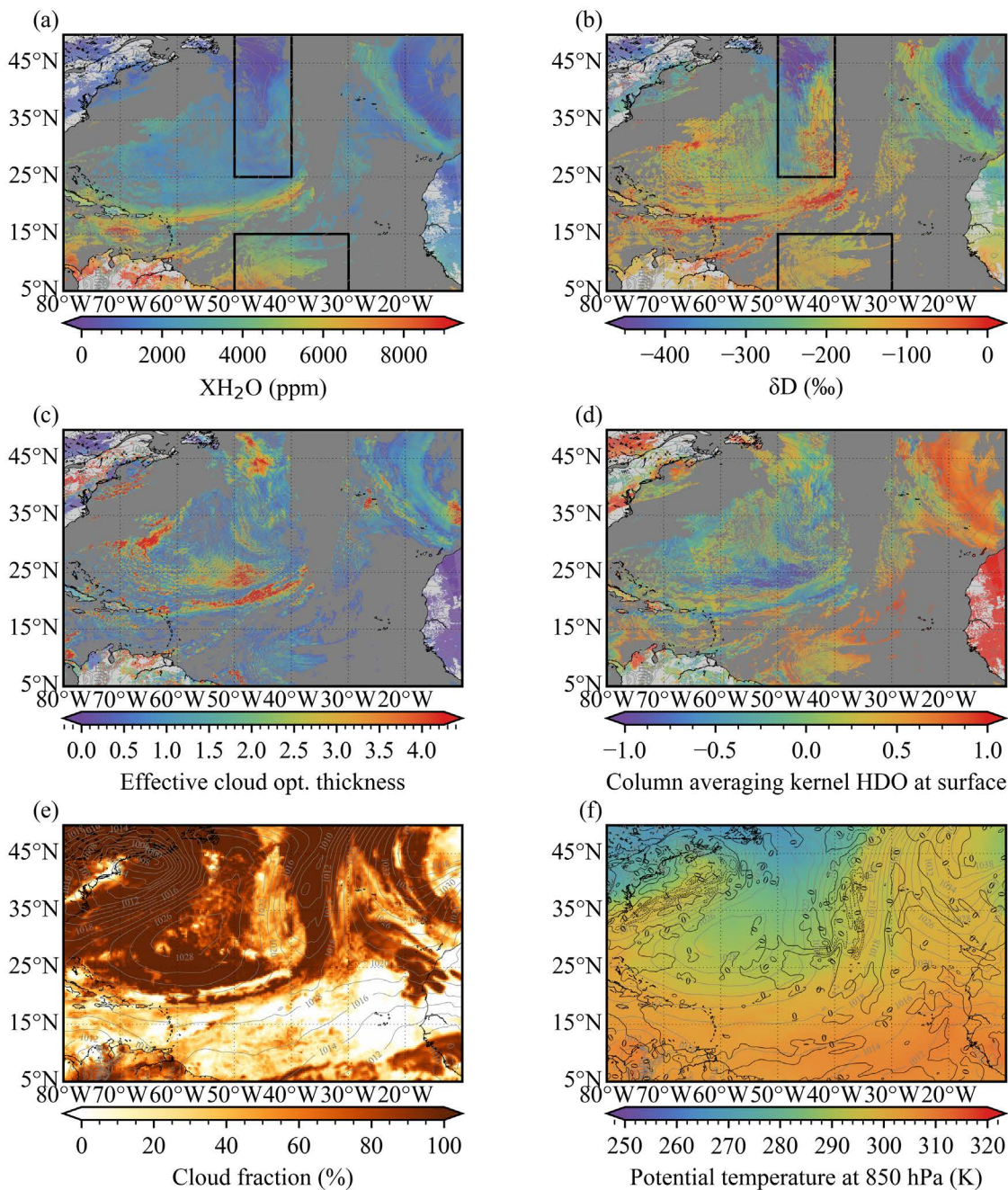


Figure 15. TROPOMI single overpass results of XH_2O (a), δD (b), retrieved effective cloud optical thickness (c) and column averaging kernel at the surface (d) over the North Atlantic on 19 Jan 2020; ERA5 cloud fraction (e) and ERA5 potential temperatures at 850 hPa at 15:00 UTC (d). The grey contours in all panels show ERA5 mean sea-level pressure at 15:00 UTC with a contour line distance of 2 hPa. The black contours in (f) show vertical winds at 500 hPa in levels of 0.5 Pa s^{-1} . The boxes in (a) and (b) mark the regions for which Rayleigh plots are depicted in Fig. 18.

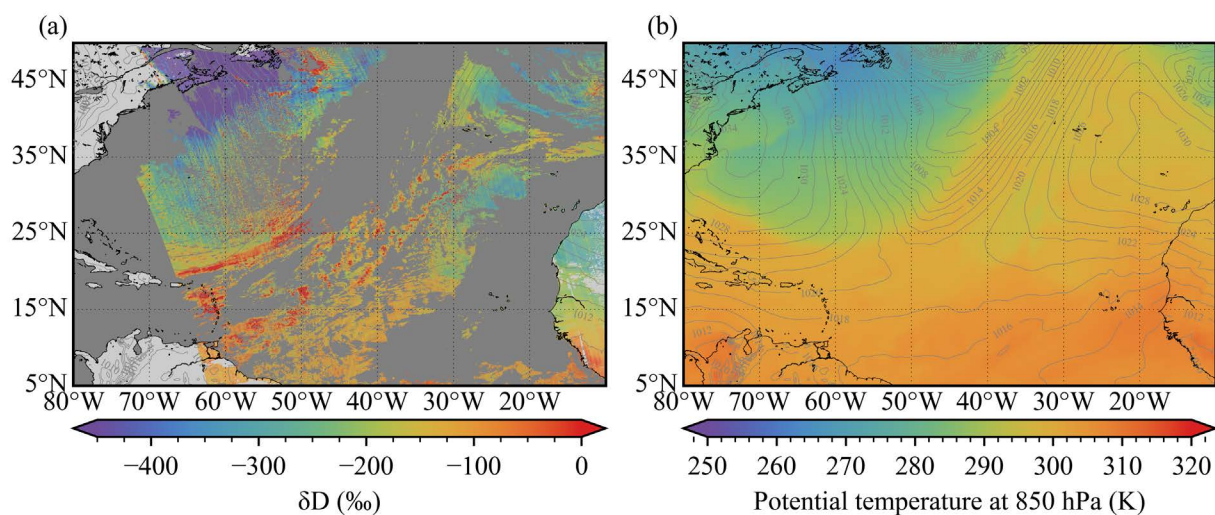


Figure 16. TROPOMI single overpass δD (a) and ERA5 potential temperatures at 850 hPa at 15:00 UTC (b) on 18 Jan 2020. The grey contours in all panels show ERA5 mean sea-level pressure at 15:00 UTC with a contour line distance of 2 hPa.

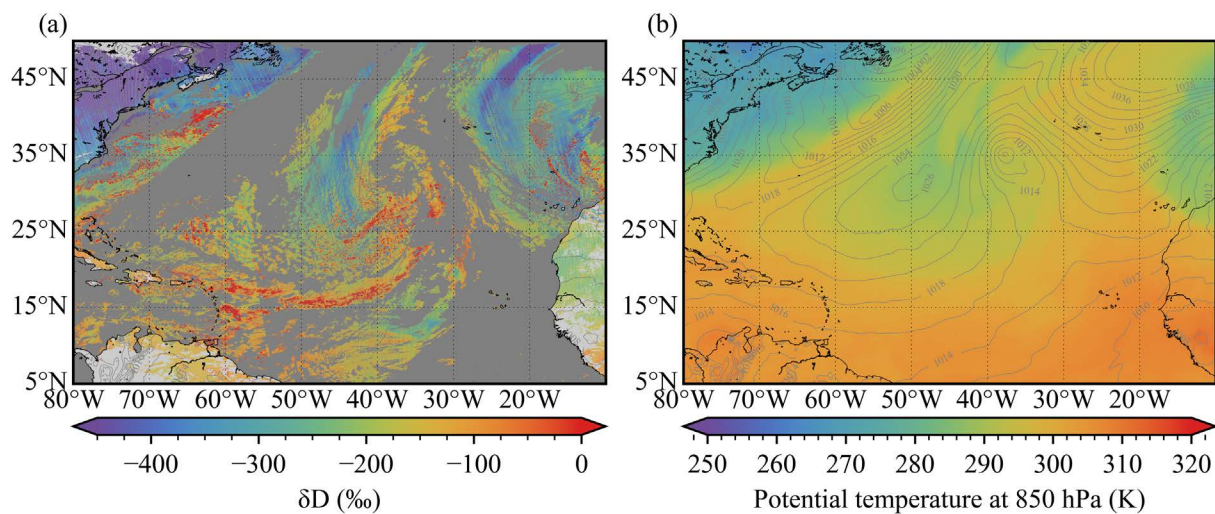


Figure 17. TROPOMI single overpass δD (a) and ERA5 potential temperatures at 850 hPa at 15:00 UTC (b) on 20 Jan 2020. The grey contours in all panels show ERA5 mean sea-level pressure at 15:00 UTC with a contour line distance of 2 hPa.

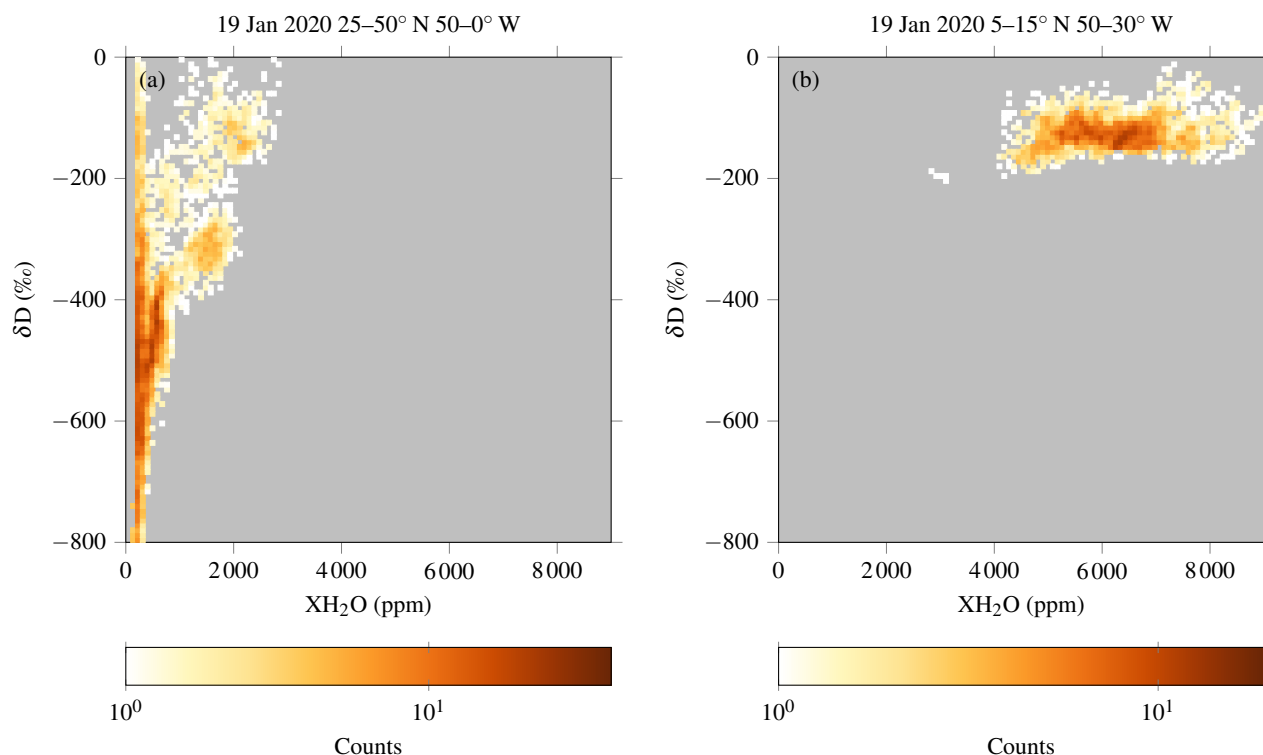


Figure 18. Histograms of TROPOMI observations on 19 Jan 2020 (a) in the area 25–50° N, 50–0° W comprising the cold sector and (b) in the area 5–15° N, 50–30° W containing the cold front.

combining TROPOMI data with high resolution numerical modelling will provide a promising data basis for studying the interaction between the moist boundary layer and the subsiding dry free tropospheric air, which is key in determining the variability in the low-level cloud cover properties.

6 Summary and conclusions

375 This work presents a new data set of H₂O and HDO columns over cloudy or clear-sky scenes retrieved from TROPOMI short-wave infrared measurements. Effective cloud parameters are fitted in the spectral window 2310 nm to 2338 nm and taken over to the final fit of the trace gases in the spectral window 2354.0 nm to 2380.5 nm. Surface albedos are regularised to the one-year average of the non-scattering retrieval by Schneider et al. (2020).

380 The performance of the new retrieval is similar to that of the non-scattering retrieval when comparing the same ground pixels, i. e. clear-sky scenes over land. Nevertheless, the scattering retrieval yields much more data, even for scenes classified as clear-sky since the filtering is less strict. The median bias to TCCON at low-altitude stations in low and middle latitudes is for clear-sky scenes 1.3×10^{21} molec cm⁻² (1.8 %) in H₂O columns, 2.0×10^{16} molec cm⁻² (-0.3 %) in HDO columns and



385 -8% (4.6 %) in a posteriori δD , the one for cloudy scenes is 4.7×10^{21} molec cm^{-2} (8.8 %) in H_2O , 1.0×10^{18} molec cm^{-2} (6.5 %) in HDO columns and -20% (12 %) in δD . At high latitudes, the bias is higher (up to about 20 % in the columns and 40 % in a posteriori δD) due to difficult measurement geometries with typically high solar zenith angles and low surface albedos meaning low signal-to-noise ratios.

390 At high-altitude stations, the altitude difference between satellite ground pixel and FTIR instrument has to be taken into account. If not corrected for, different partial columns are compared which leads to high biases. A correction by taking the partial column of the satellite observation above the ground station height largely reduces the biases in the H_2O and HDO columns, however the bias in a posteriori δD remains because the correction cancels out when using the same profile shapes. This bias can be eliminated by using the shielding of clouds: for cloudy scenes with cloud height similar to the station height, the bias in a posteriori δD is very low. This shows that the shielding by clouds provides information about the vertical distribution. For clear-sky observations, the bias in δD can be eliminated by using more realistic profile shapes for HDO: an experiment with a prior profile of HDO computed from an assumed more realistic profile of δD shows a low bias in a posteriori δD after
395 the altitude correction.

Over oceans, the retrievals are validated with aircraft profile measurements from 2018. Although the validation is hampered by a limited amount of reference measurements, the good retrieval performance is confirmed.

400 The amount of data in the new data set is tremendously increased compared to the non-scattering retrieval by Schneider et al. (2020). Besides more data for clear-sky scenes over land due to less strict filtering, retrievals over low clouds give new insights, particularly over oceans where the non-scattering retrieval cannot yield data. Single overpasses yield meaningful results which enables new case studies. As an example with cloudy scenes over the oceans, a cold air outbreak in January 2020 is shown. Retrievals from consecutive days nicely show the transport of depleted continental air from high to subtropical latitudes.

405 More reference measurements over oceans, either aircraft or ship based, will be useful to complement the validation. Furthermore, a calibration of the TCCON HDO product would be beneficial. Moreover, a homogenisation of the ground-based data products by TCCON and MUSICA-NDACC would be valuable.

Data availability. The TROPOMI HDO data set of this study is available for download at ftp://ftp.sron.nl/open-access-data-2/TROPOMI/tropomi/hdo/10_3/. TCCON data are available from the TCCON Data Archive at <https://tccodata.org/>. MUSICA data are available from <ftp://ftp.cpc.ncep.noaa.gov/ndacc/MUSICA/> or from <https://doi.org/10.5281/zenodo.48902> (Barthlott et al., 2016). Aircraft-based WISPER data from the ORACLES 2018 campaign are available from <https://espoarchive.nasa.gov/archive/browse/oracles/P3/mrg1>.

410 *Author contributions.* AS prepared the manuscript with contributions from all co-authors. FA performed the case study in Sec. 5.2. DN and DH provided aircraft data. RK provided TCCON data.



Competing interests. The authors declare that they have no conflict of interest.

Disclaimer. Plots/data contain modified Copernicus Sentinel data, processed by SRON.

Acknowledgements. This work was supported by the ESA Living Planet Fellowship project Water vapour Isotopologues from TROPOMI
415 (WIFT). The TROPOMI data processing was carried out on the Dutch national e-infrastructure with the support of the SURF Cooperative.
Kimberly Strong, Justus Notholt, Debra Wunch, Christof Petri, Nicholas Deutscher, Frank Hase, Yao Té, Thorsten Warneke, Ralf Sussmann,
Paul Wennberg, Isamu Morino, Laura T. Iraci, Kei Shiomi, Matthias Schneider, David Griffith, and Dave Pollard provided TCCON data.
Matthias Schneider provided MUSICA-NDACC data.



References

- 420 Aemisegger, F. and Papritz, L.: A Climatology of Strong Large-Scale Ocean Evaporation Events. Part I: Identification, Global Distribution, and Associated Climate Conditions, *J. Climate*, 31, 7287–7312, <https://doi.org/10.1175/JCLI-D-17-0591.1>, 2018.
- Aemisegger, F., Vogel, R., Graf, P., Dahinden, F., Villiger, L., Jansen, F., Bony, S., Stevens, B., and Wernli, H.: How Rossby wave breaking modulates the water cycle in the North Atlantic trade wind region, *Weather Clim. Dynam. Discuss.*, 2020, 1–47, <https://doi.org/10.5194/wcd-2020-51>, accepted, 2020.
- 425 Barthlott, S., Schneider, M., Hase, F., Blumenstock, T., Mengistu Tsidu, G., Grutter de la Mora, M., Strong, K., Notholt, J., Mahieu, E., Jones, N., and Smale, D.: The ground-based MUSICA dataset: Tropospheric water vapour isotopologues (H_2^{16}O , H_2^{18}O and HD^{16}O) as obtained from NDACC/FTIR solar absorption spectra, <https://doi.org/10.5281/zenodo.48902>, 2016.
- Barthlott, S., Schneider, M., Hase, F., Blumenstock, T., Kiel, M., Dubravica, D., García, O. E., Sepúlveda, E., Mengistu Tsidu, G., Takele Kenea, S., Grutter, M., Plaza-Medina, E. F., Stremme, W., Strong, K., Weaver, D., Palm, M., Warneke, T., Notholt, J., Mahieu, E., Servais, C., Jones, N., Griffith, D. W. T., Smale, D., and Robinson, J.: Tropospheric water vapour isotopologue data (H_2^{16}O , H_2^{18}O , and HD^{16}O) as obtained from NDACC/FTIR solar absorption spectra, *Earth Syst. Sci. Data*, 9, 15–29, <https://doi.org/10.5194/essd-9-15-2017>, 2017.
- 430 Blumenstock, T., Hase, F., Schneider, M., García, O. E., and Sepúlveda, E.: TCCON data from Izaña (ES), Release GGG2014.R1, <https://doi.org/10.14291/TCCON.GGG2014.IZANA01.R1>, 2017.
- Borsdorff, T., Hasekamp, O. P., Wassmann, A., and Landgraf, J.: Insights into Tikhonov regularization: application to trace gas column retrieval and the efficient calculation of total column averaging kernels, *Atmos. Meas. Tech.*, 7, 523–535, <https://doi.org/10.5194/amt-7-523-2014>, 2014.
- 435 Craig, H.: Isotopic Variations in Meteoric Waters, *Science*, 133, 1702–1703, <https://doi.org/10.1126/science.133.3465.1702>, 1961a.
- Craig, H.: Standard for Reporting Concentrations of Deuterium and Oxygen-18 in Natural Waters, *Science*, 133, 1833–1834, <https://doi.org/10.1126/science.133.3467.1833>, 1961b.
- 440 Dansgaard, W.: Stable isotopes in precipitation, *Tellus*, 16, 436–468, <https://doi.org/10.3402/tellusa.v16i4.8993>, 1964.
- De Mazière, M., Thompson, A. M., Kurylo, M. J., Wild, J. D., Bernhard, G., Blumenstock, T., Braathen, G. O., Hannigan, J. W., Lambert, J.-C., Leblanc, T., McGee, T. J., Nedoluha, G., Petropavlovskikh, I., Seckmeyer, G., Simon, P. C., Steinbrecht, W., and Strahan, S. E.: The Network for the Detection of Atmospheric Composition Change (NDACC): history, status and perspectives, *Atmos. Chem. Phys.*, 18, 4935–4964, <https://doi.org/10.5194/acp-18-4935-2018>, 2018.
- 445 Deutscher, N. M., Notholt, J., Messerschmidt, J., Weinzierl, C., Warneke, T., Petri, C., and Grupe, P.: TCCON data from Białystok (PL), Release GGG2014.R2, <https://doi.org/10.14291/TCCON.GGG2014.BIALYSTOK01.R2>, 2019.
- Fletcher, J. K., Mason, S., and Jakob, C.: A Climatology of Clouds in Marine Cold Air Outbreaks in Both Hemispheres, *J. Climate*, 29, 6677–6692, <https://doi.org/10.1175/JCLI-D-15-0783.1>, 2016.
- Gordon, I., Rothman, L., Hill, C., Kochanov, R., Tan, Y., Bernath, P., Birk, M., Boudon, V., Campargue, A., Chance, K., Drouin, B., 450 Flaud, J.-M., Gamache, R., Hodges, J., Jacquemart, D., Perevalov, V., Perrin, A., Shine, K., Smith, M.-A., Tennyson, J., Toon, G., Tran, H., Tyuterev, V., Barbe, A., Császár, A., Devi, V., Furtenbacher, T., Harrison, J., Hartmann, J.-M., Jolly, A., Johnson, T., Karman, T., Kleiner, I., Kyuberis, A., Loos, J., Lyulin, O., Massie, S., Mikhailenko, S., Moazzen-Ahmadi, N., Müller, H., Naumenko, O., Nikitin, A., Polyansky, O., Rey, M., Rotger, M., Sharpe, S., Sung, K., Starikova, E., Tashkun, S., Auwera, J. V., Wagner, G., Wilzewski, J., Wcislo, P., Yu, S., and Zak, E.: The HITRAN2016 molecular spectroscopic database, *J. Quant. Spectrosc. Radiat. Transfer*, 203, 3–69, 455 <https://doi.org/10.1016/j.jqsrt.2017.06.038>, 2017.



- Griffith, D. W., Velazco, V. A., Deutscher, N. M., Paton-Walsh, C., Jones, N. B., Wilson, S. R., Macatangay, R. C., Kettlewell, G. C., Buchholz, R. R., and Riggenbach, M. O.: TCCON data from Wollongong (AU), Release GGG2014.R0, <https://doi.org/10.14291/TCCON.GGG2014.WOLLONGONG01.R0/1149291>, 2014.
- Hagemann, R., Nief, G., and Roth, E.: Absolute isotopic scale for deuterium analysis of natural waters. Absolute D/H ratio for SMOW, *Tellus*, 22, 712–715, <https://doi.org/10.3402/tellusa.v22i6.10278>, 1970.
- 460 Hase, F., Blumenstock, T., Dohe, S., Groß, J., and Kiel, M.: TCCON data from Karlsruhe (DE), Release GGG2014.R1, <https://doi.org/10.14291/TCCON.GGG2014.KARLSRUHE01.R1/1182416>, 2015.
- Henze, D., Noone, D., Toohey, D., and Rainwater, B.: Aircraft measurements of total water heavy isotope ratios during NASA ORACLES, to be submitted to *Earth Syst. Sci. Data*, 2021.
- 465 Herbin, H., Hurtmans, D., Clerbaux, C., Clarisse, L., and Coheur, P.-F.: H_2^{16}O and HDO measurements with IASI/MetOp, *Atmos. Chem. Phys.*, 9, 9433–9447, <https://doi.org/10.5194/acp-9-9433-2009>, 2009.
- Iraci, L. T., Podolske, J. R., Hillyard, P. W., Roehl, C., Wennberg, P. O., Blavier, J.-F., Landeros, J., Allen, N., Wunch, D., Zavaleta, J., Quigley, E., Osterman, G. B., Albertson, R., Dunwoody, K., and Boyden, H.: TCCON data from Edwards (US), Release GGG2014.R1, <https://doi.org/10.14291/TCCON.GGG2014.EDWARDS01.R1/1255068>, 2016.
- 470 Kawakami, S., Ohyama, H., Arai, K., Okumura, H., Taura, C., Fukamachi, T., and Sakashita, M.: TCCON data from Saga (JP), Release GGG2014.R0, <https://doi.org/10.14291/TCCON.GGG2014.SAGA01.R0/1149283>, 2014.
- Kivi, R., Heikkinen, P., and Kyrö, E.: TCCON data from Sodankylä (FI), Release GGG2014.R0, <https://doi.org/10.14291/TCCON.GGG2014.SODANKYLA01.R0/1149280>, 2014.
- Krol, M., Houweling, S., Bregman, B., van den Broek, M., Segers, A., van Velthoven, P., Peters, W., Dentener, F., and Bergamaschi, P.: The two-way nested global chemistry-transport zoom model TM5: algorithm and applications, *Atmos. Chem. Phys.*, 5, 417–432, <https://doi.org/10.5194/acp-5-417-2005>, 2005.
- 475 Lacour, J.-L., Risi, C., Clarisse, L., Bony, S., Hurtmans, D., Clerbaux, C., and Coheur, P.-F.: Mid-tropospheric δD observations from IASI/MetOp at high spatial and temporal resolution, *Atmos. Chem. Phys.*, 12, 10 817–10 832, <https://doi.org/10.5194/acp-12-10817-2012>, 2012.
- 480 Landgraf, J., aan de Brugh, J., Scheepmaker, R., Borsdorff, T., Hu, H., Houweling, S., Butz, A., Aben, I., and Hasekamp, O.: Carbon monoxide total column retrievals from TROPOMI shortwave infrared measurements, *Atmos. Meas. Tech.*, 9, 4955–4975, <https://doi.org/10.5194/amt-9-4955-2016>, 2016.
- Morino, I., Matsuzaki, T., and Horikawa, M.: TCCON data from Tsukuba (JP), 125HR, Release GGG2014.R2, <https://doi.org/10.14291/TCCON.GGG2014.TSUKUBA02.R2>, 2018a.
- 485 Morino, I., Velazco, V. A., Hori, A., Uchino, O., and Griffith, D. W.: TCCON data from Burgos, Ilocos Norte (PH), Release GGG2014.R0, <https://doi.org/10.14291/TCCON.GGG2014.BURGOS01.R0>, 2018b.
- Morino, I., Yokozeki, N., Matsuzaki, T., and Horikawa, M.: TCCON data from Rikubetsu (JP), Release GGG2014.R2, <https://doi.org/10.14291/TCCON.GGG2014.RIKUBETSU01.R2>, 2018c.
- Myers, T. A. and Norris, J. R.: Observational Evidence That Enhanced Subsidence Reduces Subtropical Marine Boundary Layer Cloudiness, *J. Climate*, 26, 7507–7524, <https://doi.org/10.1175/JCLI-D-12-00736.1>, 2013.
- 490 Noone, D.: Pairing Measurements of the Water Vapor Isotope Ratio with Humidity to Deduce Atmospheric Moistening and Dehydration in the Tropical Midtroposphere, *J. Climate*, 25, 4476–4494, <https://doi.org/10.1175/JCLI-D-11-00582.1>, 2012.



- Norris, J. R.: Low Cloud Type over the Ocean from Surface Observations. Part I: Relationship to Surface Meteorology and the Vertical Distribution of Temperature and Moisture, *J. Climate*, 11, 369–382, [https://doi.org/10.1175/1520-0442\(1998\)011<0369:LCTOTO>2.0.CO;2](https://doi.org/10.1175/1520-0442(1998)011<0369:LCTOTO>2.0.CO;2), 1998.
- 495
- Notholt, J., Petri, C., Warneke, T., Deutscher, N. M., Palm, M., Buschmann, M., Weinzierl, C., Macatangay, R. C., and Grupe, P.: TCCON data from Bremen (DE), Release GGG2014.R1, <https://doi.org/10.14291/TCCON.GGG2014.BREMEN01.R0/1149275>, 2019a.
- Notholt, J., Warneke, T., Petri, C., Deutscher, N. M., Weinzierl, C., Palm, M., and Buschmann, M.: TCCON data from Ny Ålesund, Spitsbergen (NO), Release GGG2014.R1, <https://doi.org/10.14291/TCCON.GGG2014.NYALESUND01.R1>, 2019b.
- 500 Pollard, D. F., Robinson, J., and Shiona, H.: TCCON data from Lauder (NZ), Release GGG2014.R0, <https://doi.org/10.14291/TCCON.GGG2014.LAUDER03.R0>, 2019.
- Rast, M., Johannessen, J., and Mauser, W.: Review of Understanding of Earth's Hydrological Cycle: Observations, Theory and Modelling, *Surv. Geophys.*, 35, 491–513, <https://doi.org/10.1007/s10712-014-9279-x>, 2014.
- Redemann, J., Wood, R., Zuidema, P., Doherty, S. J., Luna, B., LeBlanc, S. E., Diamond, M. S., Shinozuka, Y., Chang, I. Y., Ueyama, R., Pfister, L., Ryoo, J.-M., Dobracki, A. N., da Silva, A. M., Longo, K. M., Kacenelenbogen, M. S., Flynn, C. J., Pistone, K., Knox, N. M., Piketh, S. J., Haywood, J. M., Formenti, P., Mallet, M., Stier, P., Ackerman, A. S., Bauer, S. E., Fridlind, A. M., Carmichael, G. R., Saide, P. E., Ferrada, G. A., Howell, S. G., Freitag, S., Cairns, B., Holben, B. N., Knobelspiesse, K. D., Tanelli, S., L'Ecuyer, T. S., Dzambo, A. M., Sy, O. O., McFarquhar, G. M., Poellot, M. R., Gupta, S., O'Brien, J. R., Nenes, A., Kacarab, M., Wong, J. P. S., Small-Griswold, J. D., Thornhill, K. L., Noone, D., Podolske, J. R., Schmidt, K. S., Pilewskie, P., Chen, H., Cochrane, S. P., Sedlacek, A. J., Lang, T. J., Stith, E., Segal-Rozenhaimer, M., Ferrare, R. A., Burton, S. P., Hostetler, C. A., Diner, D. J., Seidel, F. C., Platnick, S. E., Myers, J. S., Meyer, K. G., Spangenberg, D. A., Maring, H., and Gao, L.: An overview of the ORACLES (ObseRvations of Aerosols above CLouds and their intERactionS) project: aerosol–cloud–radiation interactions in the southeast Atlantic basin, *Atmos. Chem. Phys.*, 21, 1507–1563, <https://doi.org/10.5194/acp-21-1507-2021>, 2021.
- 505
- Scheepmaker, R. A., aan de Brugh, J., Hu, H., Borsdorff, T., Frankenberg, C., Risi, C., Hasekamp, O., Aben, I., and Landgraf, J.: HDO and H₂O total column retrievals from TROPOMI shortwave infrared measurements, *Atmos. Meas. Tech.*, 9, 3921–3937, <https://doi.org/10.5194/amt-9-3921-2016>, 2016.
- 515
- Schneider, A., Borsdorff, T., aan de Brugh, J., Hu, H., and Landgraf, J.: A full-mission data set of H₂O and HDO columns from SCIAMACHY 2.3 μm reflectance measurements, *Atmos. Meas. Tech.*, 11, 3339–3350, <https://doi.org/10.5194/amt-11-3339-2018>, 2018.
- Schneider, A., Borsdorff, T., aan de Brugh, J., Aemisegger, F., Feist, D. G., Kivi, R., Hase, F., Schneider, M., and Landgraf, J.: First data set of H₂O/HDO columns from the Tropospheric Monitoring Instrument (TROPOMI), *Atmos. Meas. Tech.*, 13, 85–100, <https://doi.org/10.5194/amt-13-85-2020>, 2020.
- 520
- Schneider, M. and Hase, F.: Optimal estimation of tropospheric H₂O and δD with IASI/METOP, *Atmos. Chem. Phys.*, 11, 11 207–11 220, <https://doi.org/10.5194/acp-11-11207-2011>, 2011.
- Schneider, M., Wiegeler, A., Barthlott, S., González, Y., Christner, E., Dyroff, C., García, O. E., Hase, F., Blumenstock, T., Sepúlveda, E., Mengistu Tsidu, G., Takele Kenea, S., Rodríguez, S., and Andrey, J.: Accomplishments of the MUSICA project to provide accurate, long-term, global and high-resolution observations of tropospheric {H₂O,δD} pairs – a review, *Atmos. Meas. Tech.*, 9, 2845–2875, <https://doi.org/10.5194/amt-9-2845-2016>, 2016.
- 525
- Sherlock, V., Connor, B., Robinson, J., Shiona, H., Smale, D., and Pollard, D. F.: TCCON data from Lauder (NZ), 125HR, Release GGG2014.R0, <https://doi.org/10.14291/TCCON.GGG2014.LAUDER02.R0/1149298>, 2014.
- 530
- Stevens, B. and Bony, S.: What Are Climate Models Missing?, *Science*, 340, 1053–1054, <https://doi.org/10.1126/science.1237554>, 2013.



- Strong, K., Roche, S., Franklin, J. E., Mendonca, J., Lutsch, E., Weaver, D., Fogal, P. F., Drummond, J. R., Batchelor, R., and Lindenmaier, R.: TCCON data from Eureka (CA), Release GGG2014.R3, <https://doi.org/10.14291/TCCON.GGG2014.EUREKA01.R3>, 2019.
- Sussmann, R. and Rettinger, M.: TCCON data from Garmisch (DE), Release GGG2014.R2, <https://doi.org/10.14291/TCCON.GGG2014.GARMISCH01.R2>, 2018a.
- 535 Sussmann, R. and Rettinger, M.: TCCON data from Zugspitze (DE), Release GGG2014.R1, <https://doi.org/10.14291/TCCON.GGG2014.ZUGSPITZE01.R1>, 2018b.
- Thurnherr, I., Hartmuth, K., Jansing, L., Gehring, J., Boettcher, M., Gorodetskaya, I., Werner, M., Wernli, H., and Aemisegger, F.: The role of air–sea fluxes for the water vapour isotope signals in the cold and warm sectors of extratropical cyclones over the Southern Ocean, *Weather Clim. Dynam. Discuss.*, 2020, 1–42, <https://doi.org/10.5194/wcd-2020-46>, under review, 2020a.
- 540 Thurnherr, I., Kozachek, A., Graf, P., Weng, Y., Bolshiyakov, D., Landwehr, S., Pfahl, S., Schmale, J., Sodemann, H., Steen-Larsen, H. C., Toffoli, A., Wernli, H., and Aemisegger, F.: Meridional and vertical variations of the water vapour isotopic composition in the marine boundary layer over the Atlantic and Southern Ocean, *Atmos. Chem. Phys.*, 20, 5811–5835, <https://doi.org/10.5194/acp-20-5811-2020>, 2020b.
- Té, Y., Jeseck, P., and Janssen, C.: TCCON data from Paris (FR), Release GGG2014.R0, <https://doi.org/10.14291/TCCON.GGG2014.PARIS01.R0/1149279>, 2014.
- 545 Veefkind, J. P., Aben, I., McMullan, K., Förster, H., de Vries, J., Otter, G., Claas, J., Eskes, H. J., de Haan, J. F., Kleipool, Q., van Weele, M., Hasekamp, O., Hoogeveen, R., Landgraf, J., Snel, R., Tol, P., Ingmann, P., Voors, R., Kruizinga, B., Vink, R., Visser, H., and Levelt, P. F.: TROPOMI on the ESA Sentinel-5 Precursor: A GMES mission for global observations of the atmospheric composition for climate, air quality and ozone layer applications, *Remote Sens. Environ.*, 120, 70–83, <https://doi.org/10.1016/j.rse.2011.09.027>, 2012.
- 550 Warneke, T., Messerschmidt, J., Notholt, J., Weinzierl, C., Deutscher, N. M., Petri, C., and Grupe, P.: TCCON data from Orléans (FR), Release GGG2014.R1, <https://doi.org/10.14291/TCCON.GGG2014.ORLEANS01.R1>, 2019.
- Wennberg, P. O., Wunch, D., Roehl, C. M., Blavier, J.-F., Toon, G. C., and Allen, N. T.: TCCON data from Caltech (US), Release GGG2014.R1, <https://doi.org/10.14291/TCCON.GGG2014.PASADENA01.R1/1182415>, 2015.
- 555 Wennberg, P. O., Roehl, C. M., Blavier, J.-F., Wunch, D., and Allen, N. T.: TCCON data from Jet Propulsion Laboratory (US), 2011, Release GGG2014.R1, <https://doi.org/10.14291/TCCON.GGG2014.JPL02.R1/1330096>, 2016a.
- Wennberg, P. O., Wunch, D., Roehl, C. M., Blavier, J.-F., Toon, G. C., and Allen, N. T.: TCCON data from Lamont (US), Release GGG2014.R1, <https://doi.org/10.14291/TCCON.GGG2014.LAMONT01.R1/1255070>, 2016b.
- Wennberg, P. O., Roehl, C. M., Wunch, D., Toon, G. C., Blavier, J.-F., Washenfelder, R., Keppel-Aleks, G., Allen, N. T., and Ayers, J.: TCCON data from Park Falls (US), Release GGG2014.R1, <https://doi.org/10.14291/TCCON.GGG2014.PARKFALLS01.R1>, 2017.
- 560 Wernli, H. and Schwierz, C.: Surface Cyclones in the ERA-40 Dataset (1958–2001). Part I: Novel Identification Method and Global Climatology, *J. Atmos. Sci.*, 63, 2486–2507, <https://doi.org/10.1175/JAS3766.1>, 2006.
- Worden, J., Kulawik, S., Frankenberg, C., Payne, V., Bowman, K., Cady-Peirara, K., Wecht, K., Lee, J.-E., and Noone, D.: Profiles of CH₄, HDO, H₂O, and N₂O with improved lower tropospheric vertical resolution from Aura TES radiances, *Atmos. Meas. Tech.*, 5, 397–411, <https://doi.org/10.5194/amt-5-397-2012>, 2012.
- 565 Worden, J. R., Kulawik, S. S., Fu, D., Payne, V. H., Lipton, A. E., Polonsky, I., He, Y., Cady-Pereira, K., Moncet, J.-L., Herman, R. L., Irion, F. W., and Bowman, K. W.: Characterization and evaluation of AIRS-based estimates of the deuterium content of water vapor, *Atmos. Meas. Tech.*, 12, 2331–2339, <https://doi.org/10.5194/amt-12-2331-2019>, 2019.



- 570 Wunch, D., Toon, G. C., Blavier, J.-F. L., Washenfelder, R. A., Notholt, J., Connor, B. J., Griffith, D. W. T., Sherlock, V., and Wennberg, P. O.: The Total Carbon Column Observing Network, *Philos. T. Roy. Soc. A*, 369, 2087–2112, <https://doi.org/10.1098/rsta.2010.0240>, 2011.
- Wunch, D., Mendonca, J., Colebatch, O., Allen, N. T., Blavier, J.-F., Roche, S., Hedelius, J., Neufeld, G., Springett, S., Worthy, D., Kessler, R., and Strong, K.: TCCON data from East Trout Lake, SK (CA), Release GGG2014.R1, <https://doi.org/10.14291/TCCON.GGG2014.EASTTROUTLAKE01.R1>, 2018.
- 575 Zdunkowski, W. G., Welch, R. M., and Korb, G.: An Investigation of the Structure of Typical Two-stream-methods for the Calculation of Solar Fluxes and Heating Rates in Clouds, *Contrib. Atmos. Phys.*, 53, 147–166, 1980.